mathematics

MDPI

Article

Closed-Form Design Quantiles Under Skewness and Kurtosis: A Hermite Approach to Structural Reliability

Zdeněk Kala

Institute of Structural Mechanics, Faculty of Civil Engineering, Brno University of Technology, 602 00 Brno, Czech Republic; zdenek.kala@vut.cz or kala.z@fce.vutbr.cz

Abstract

A Hermite-based framework for reliability assessment within the limit state method is developed in this paper. Closed-form design quantiles under a four-moment Hermite density are derived by inserting the Gaussian design quantile into a calibrated cubic translation. Admissibility and implementation criteria are established, including a monotonicity bound, a positivity condition for the platykurtic branch, and a balanced Jacobian condition for the leptokurtic branch. Material data for the yield strength and ductility of structural steel are fitted using moment-matched Hermite models and validated through goodness-of-fit tests. A truss structure is subsequently analysed to quantify how non-Gaussian input geometry influences structural resistance and its associated design value. Variance-based Sobol sensitivity analysis shows that departures of the radius distribution toward negative skewness and higher kurtosis increase the first-order contribution of geometric variables and thicken the lower tail of the resistance distribution. The closed-form Hermite design resistances agree closely with numerical integration results and reveal systematic deviations from FORM estimates, which depend solely on the mean and standard deviation. Monte Carlo simulations confirm these trends and highlight the slow convergence of tail quantiles and higher-order moments. The proposed approach remains fully compatible in the Gaussian limit and offers a practical complement to EN 1990 verification procedures when skewness and kurtosis have a significant influence on design quantiles.

Keywords: Hermite distribution; structural reliability; design quantiles; limit states method; first-order reliability method; non-Gaussian modelling; skewness; kurtosis; Sobol sensitivity analysis; Monte Carlo simulation

MSC: 65C50; 60H99; 82B31

Academic Editors: Ioannis S. Triantafyllou and Alex Karagrigoriou

Received: 14 November 2025
Revised: 15 December 2025
Accepted: 21 December 2025
Published: 24 December 2025

1. Introduction

EN 1990 [1] adopts a simplified approach to structural reliability in which only the mean and standard deviation are used to determine design values through the First-Order Reliability Method (FORM). The Standard [1] introduces three basic probability distributions, namely Gaussian, lognormal, and Gumbel, together with their probability density functions (PDFs). Structural resistance is most often modelled using Gaussian [2,3] or lognormal [4,5] PDFs, whereas the Gumbel PDF is used to represent extremes of dynamic response [6,7] or long-term, single-variable load actions [8–11].

In practice, EN 1990 does not prescribe specific mappings between variables and probability distributions. It provides closed-form design expressions only for these three two-parameter families, see Figure 1. The target reliability must therefore be demonstrated

using a distribution and parameter values that reproduce the observed data. However, two-parameter PDFs may be inadequate for this purpose, see, e.g., [12–14].

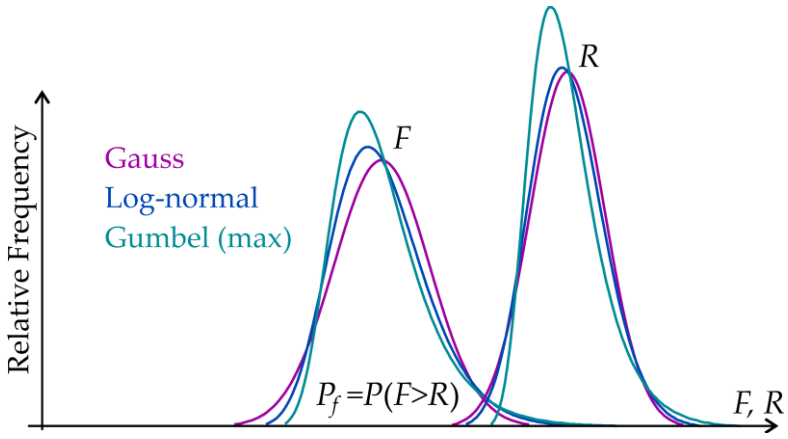

Figure 1. Schematic comparison of two-parameter distributions given in EN 1990, applied to load F and resistance R. The choice of PDF affects the value of failure probability $P_f = P(F > R)$.

Numerous studies have shown that the actual probability distribution of structural resistance often departs from idealised Gaussian or lognormal models [15,16]. For example, recent material tests indicate that different failure modes or material properties may follow distinct distributions—tensile strength may fit a normal law, whereas compression or shear strength may follow Weibull or lognormal laws [15]. Strength data for high-performance fibres and polymers further show that, even when statistical tests "cannot reject normality", the true strength histograms visibly deviate from the ideal bell-shaped Gaussian curve [16]. Manufacturing defects in advanced composite materials can produce fat-tailed or skewed resistance distributions rather than the assumed thin-tailed form [17]. Similarly, accelerated ageing or damage may shift an initially normal resistance distribution toward a Weibull-type distribution with heavier tails [18]. In such cases, structural strength variables exhibit skewness, heavy tails, or even multimodal behaviour, departing significantly from the classical normal or lognormal assumptions [17,18].

There are measurement cases in which the data distribution is only approximately Gaussian. However, when slightly larger deviations characterised by higher skewness or kurtosis occur, alternative distribution models should be considered [19,20]. Such cases have been observed both in experimental data [21,22] and in outputs of engineering models [23,24]. In these cases, the histogram approaches a bell curve, and the higher moments (skewness and kurtosis) approach zero or small values typical of a normal distribution. A suitable representation in such circumstances is the four-parameter Hermite PDF [25].

This article analyses the limit states of load-bearing structures using a Hermite model [25], calibrated to measured data exhibiting non-negligible skewness and kurtosis. Emphasis is placed on cases where the shape of the probability distribution substantially influences the lower design quantiles of resistance and, consequently, the required level of reliability. Sobol sensitivity analysis is employed to quantify the contribution of each input variable and their interactions to the variance of the model output. In addition, it is used to evaluate how different choices of input probability distributions affect overall model sensitivity.

2. Hermite Models for Tail-Sensitive Reliability

Many studies report that the probability distributions of load and resistance variables deviate from the Gaussian law and can exhibit non-zero skewness and kurtosis [26–29]. These higher-order moments may significantly influence failure probabilities and the

reliability index [30,31]. Consequently, computed results may depend on the assumed input distributions, as demonstrated, for example, for truss towers subjected to wind loading [32]. More advanced probabilistic models are therefore required.

The Hermite translation method serves as a tail-aware default when departure from normality is of interest. Its third-order mapping transforms a Gaussian variable into a non-Gaussian one, with shape parameters controlling skewness and kurtosis [25,33,34]. Evidence from wind engineering shows that the Hermite PDF improves tail representation for both mildly and strongly non-Gaussian pressure data on low-rise buildings [35]. The Hermite PDF has also been employed to estimate moment-based peak factors for pressure and displacement responses [36,37]. When full probability distributions are unavailable, reliability assessment and partial safety factor calibration can utilise moment methods based on the third to fifth moments [30,31,38]. Correlated inputs can be addressed using an L-moment-based normal transformation [39]. These approaches do not require full distributions and capture non-Gaussian behaviour more faithfully. As a general alternative, a unimodal four-moment density can represent a wide range of skewness and kurtosis and connects to both normal and lognormal limits [40].

Extensions of Hermite models target small to moderate deviations from normality. An adaptive Hermite model using probability-weighted moments estimates extreme value distributions for seismic reliability, while asymptotic analysis clarifies the monotonic domain and establishes connections to Gram–Charlier behaviour [41,42]. L-moment-based Hermite mappings enable efficient simulation of non-Gaussian random fields in structural [43] and geotechnical applications [44]. When higher-order moments are required but full distributions are not available, skewness and kurtosis can be estimated through a regression-based adaptation of the Cornish–Fisher expansion to improve shape recovery for asymmetric or heavy-tailed data [45]. In parallel, a flexible four-moment distribution employing a cubic normal transformation covers a broad region of the skewness–kurtosis plane and connects to the normal and lognormal limits [46]. For non-stationary, non-Gaussian responses, a unified Hermite mapping provides analytical mean upcrossing rates, and complementary studies quantify the transmission of kurtosis from excitation to response under both stationary and non-stationary loadings [47–50]. Hermite polynomial models have also been integrated into dynamic reliability formulations under non-Gaussian excitation [51].

Fatigue assessment is particularly sensitive to non-Gaussian features, as damage accumulation is driven by high-amplitude cycles in the distribution tails. Skewness and kurtosis can be embedded into damage estimators through Hermite-based mappings when full distributions are unavailable. For instance, Hermite transformations have been applied to fatigue damage estimation in broadband non-Gaussian processes using a conditional probability approach [52]. Time–frequency frameworks for non-stationary loading employ spectral methods for non-Gaussian processes and support fatigue evaluation [53]. Fast modal-domain estimators of response kurtosis enable efficient assessment of non-Gaussian effects in full finite element models used for random vibration fatigue [54]. Under simultaneous non-Gaussian processes, bias correction incorporating kurtosis improves fatigue damage estimates compared with linear summation [55]. For floating offshore wind turbine blades, non-Gaussian wind fields have been shown to reduce predicted fatigue life relative to Gaussian assumptions [56].

Direct applications of the Hermite PDF, or its explicit use for uncertainty modelling, span theoretical developments [33,34,41,42,47], simulation and random fields [43,44,57], wind loading and peak factor estimation [35–37,58], and reliability and fatigue analysis [25,51,52,56]. Several studies have employed quartic-order Hermite polynomial mappings to transform Gaussian variables into prescribed non-Gaussian distributions [31,44,57,58]. Although the quartic Hermite polynomial can provide finer control over the PDF shape, its monotonic

domain is assessed locally and may be narrower over the practical working range. In contrast, the cubic Hermite PDF model used in this study provides a transparent and easily verifiable monotonic boundary [44,58]. The cubic model is suitable for formulating design quantiles and can surpass the accuracy of design values obtained using the classical FORM.

3. Hermite Model: Map, Densities, and Properties

The Hermite translation model is introduced to represent moderate deviations from Gaussian behaviour while maintaining a compact four-parameter description defined by the mean, standard deviation, skewness, and kurtosis [25]. Throughout this chapter, a real-valued random variable X with finite moments is considered. The mean and variance are denoted by μ and σ^2. The central and standardised moments follow the conventions stated below.

$$\mu = E(X),\ \ \sigma^2 = V(X),\ \ \mu_r^c = E\big((X-\mu)^r\big),\ r \geq 1. \tag{1}$$

$$\alpha_3 = \frac{\mu_3^c}{\sigma^3},\ \ \alpha_4 = \frac{\mu_4^c}{\sigma^4}. \tag{2}$$

For a Gaussian variable, one has $\alpha_4 = 3$; departures from Gaussian kurtosis are therefore captured by $\alpha_4 - 3$. Under these conventions, the standardisation in Equation (3) maps the observations to zero mean and unit variance, while the Hermite translation in Equation (4) introduces controlled adjustments to symmetry and tail weight through the calibrated coefficients defined in Equations (5), (6) and (14).

3.1. Polynomial Map and Parameterisation

A random variable X with mean μ, standard deviation σ, skewness α_3, and excess kurtosis α_4 is approximated by transforming a standard normal variable $U \sim N(0, 1)$.

The standardised observation is

$$y = \frac{x-\mu}{\sigma}. \tag{3}$$

Equation (3) maps the physical variable x to the standardised variable y with zero mean and unit variance, which is a necessary prerequisite for applying the Hermite translation in Equation (4). The Hermite translation model introduces a unit-variance surrogate defined as

$$Y = k\Big[U + h_3\Big(U^2 - 1\Big) + h_4\Big(U^3 - 3U\Big)\Big], \tag{4}$$

where $H_2(U) = U^2 - 1$ and $H_3(U) = U^3 - 3U$ are the second- and third-order Hermite polynomials, respectively. Equation (4) introduces a cubic translation of the standard normal variable U, in which the Hermite terms modify the symmetry and tail behaviour according to the prescribed skewness α_3, and excess kurtosis α_4. The scaling factor k compensates for the variance modification introduced by the Hermite terms, ensuring that $V(Y) = 1$ is preserved. The third- and fourth-order base coefficients h_3 and h_4 are given by

$$h_3 = \frac{\alpha_3}{6},\ h_4 = \frac{\alpha_4 - 3}{24}, \tag{5}$$

where the constant k is a variance rescaling factor chosen such that $V(Y) = 1$. Because the Hermite polynomials are orthogonal under the Gaussian inner product, $E[U\,H_n(U)] = 0$, the centring is preserved, i.e., $E(Y) = 0$. Equations (3)–(5) define the common basis of the model. The branch-specific calibrations $\widetilde{h}_3$, $\widetilde{h}_4$ and correction factors k_t are introduced below. The untilded coefficients h_3 and h_4 are directly linked to the target skewness and kurtosis (α_3, α_4), whereas the calibrated quantities $\widetilde{h}_3$, $\widetilde{h}_4$ and k_t are the adjusted parameters actually used in the PDF evaluation to enforce variance normalisation and branch-dependent admissibility.

The forward transformation is now fully specified, and Section 3.2 derives the corresponding probability density function via inversion of Equation (4).

3.2. Density Derivations

3.2.1. Lower-Branch Density ($\alpha_4 \leq 3$)

For $\alpha_4 \leq 3$, the Winterstein calibration is applied:

$$\widetilde{h}_4 = h_4 - 27h_4^2, \;\; \widetilde{h}_3 = \frac{h_3}{1 + 24\widetilde{h}_4}, \;\; k_t = \frac{1}{\sqrt{1 + 10\widetilde{h}_3^2 + 42\widetilde{h}_4^2}}. \tag{6}$$

This Winterstein correction re-parameterises the original coefficients h_3 and h_4 into $\widetilde{h}_3$, $\widetilde{h}_4$ and k_t such that the mapping preserves unit variance, reproduces the target skewness and kurtosis, and remains monotonic for $\alpha_4 \leq 3$ [25].

Dividing Equation (4) by k_t gives the working, dimensionless mapping:

$$y = \frac{Y}{k_t} = U + \widetilde{h}_3\left(U^2 - 1\right) + \widetilde{h}_4\left(U^3 - 3U\right), \tag{7}$$

The density of Y follows from the change-of-variables formula:

$$f_Y(y) = \phi(U(y)) \cdot \left|\frac{dU}{dy}\right|, \; \phi(u) = \frac{1}{\sqrt{2\pi}} e^{\frac{-u^2}{2}}, \tag{8}$$

and is obtained perturbatively for $\left|\widetilde{h}_3\right|, \left|\widetilde{h}_4\right| \ll 1$.

To obtain the PDF $f_Y(y)$, the mapping in Equation (7) must be inverted. For $\left|\widetilde{h}_3\right|$, $\left|\widetilde{h}_4\right| \ll 1$, a first-order Neumann expansion provides an explicit approximation of the inverse $U(y)$, using $(1 + a)^{-1} \approx 1 - a$ for $|a| \ll 1$. Applying this procedure and retaining only first-order terms yields Equation (9):

$$U(y) \approx y - \widetilde{h}_3\left(y^2 - 1\right) - \widetilde{h}_4\left(y^3 - 3y\right). \tag{9}$$

Differentiating Equation (7) with respect to U and replacing $U \approx y$ in first order yields the Jacobian shown in Equation (10):

$$\frac{dy}{dU} = 1 + 2\widetilde{h}_3 U + 3\widetilde{h}_4\left(U^2 - 1\right) \;\Rightarrow\; \left|\frac{dU}{dy}\right| \approx 1 - 2\widetilde{h}_3 y - 3\widetilde{h}_4\left(y^2 - 1\right), \tag{10}$$

where U is replaced by y at first order. Substituting the approximate inverse from Equation (9) and the Jacobian from Equation (10) into the change-of-variables formula (Equation (8)) gives the first-order density in Equation (11):

$$f_Y(y) \approx \phi(U(y)) \cdot \left|1 - 2\widetilde{h}_3 y - 3\widetilde{h}_4\left(y^2 - 1\right)\right|. \tag{11}$$

For a non-standardised X, it is convenient (and consistent with the calibration) to evaluate the model at:

$$y = \frac{x - \mu}{\sigma\, k_t}, \tag{12}$$

whence, by the one-dimensional change-of-variables rule,

$$f_X(x) = \frac{1}{\sigma\, k_t} f_Y\left(\frac{x - \mu}{\sigma\, k_t}\right). \tag{13}$$

Equations (9)–(13) define the lower-branch PDF used in practical applications. The approximation remains accurate while $|\alpha_3| \ll 1$ and the kurtosis surplus $\alpha_4 - 3$ is non-positive or only mildly positive.

3.2.2. Upper-Branch Density ($\alpha_4 > 3$)

For $\alpha_4 > 3$, the first-order lower-branch representation is no longer sufficient, and the exact upper-branch formulation is used. The calibration in Equation (14) ensures unit variance and allows for larger excess kurtosis.

$$\widetilde{h}_4 = \frac{\sqrt{1+36h_4}-1}{18},\ \widetilde{h}_3 = \frac{h_3}{1+6\widetilde{h}_4},\ k_t = \frac{1}{\sqrt{1+2\widetilde{h}_3^2+6\widetilde{h}_4^2}}. \tag{14}$$

The working mapping remains as given in Equation (7), with $\widetilde{h}_3$, $\widetilde{h}_4$ and k_t obtained from Equation (14). For $\alpha_4 > 3$, the parameters $\widetilde{h}_3$ and $\widetilde{h}_4$ can be obtained exactly by inverting Equations (31) and (32) when the target moments (α_3^*, α_4^*) are prescribed. If $\widetilde{h}_3$ and $\widetilde{h}_4$ are exact, then Equation (14) gives the exact variance-scaling factor k_t.

In this branch, the inverse mapping $U(y)$ can be obtained in the closed form. To enable a closed-form inversion of the cubic mapping in Equation (7), the transformation in Equation (15) introduces the auxiliary quantities A, B, Q and ξ, chosen such that a subsequent shift in variables removes the quadratic term and reduces the polynomial to a depressed cubic.

$$B = \frac{1}{3\widetilde{h}_4},\ \ A = \widetilde{h}_3 B,\ \ Q = B - 1 - A^2,\ \ \xi = \frac{3}{2}B(A+y) - A^3. \tag{15}$$

Introducing the shift $U = X - A$ and substituting it into Equation (7) eliminates the quadratic term and yields the depressed form. The purpose of this shift is to centre the polynomial at its inflection point (so that the inflection point is located at $X = 0$), which algebraically cancels the X^2 term. This yields the depressed form:

$$X^3 + 3QX - 2\xi = 0, \tag{16}$$

where the coefficients Q and ξ are those defined in Equation (15). A step-by-step algebraic verification of this reduction, starting from Equation (7), is provided in Appendix A, where the cancellation of the quadratic term is shown.

Define

$$R = \sqrt{\xi^2 + Q^3}, \cdot (\geq |\xi|). \tag{17}$$

Applying Cardano's formula for the real root of the depressed cubic in Equation (16) provides the explicit inverse mapping $U(y)$ given in Equation (18).

$$U(y) = \sqrt[3]{R+\xi} - \sqrt[3]{R-\xi} - A. \tag{18}$$

This expression for $U(y)$ satisfies Equation (16) (with $X = U + A$) and, consequently, the original mapping in Equation (7).

The Jacobian dU/dy is obtained by differentiating Equation (18). From Equations (15) and (17),

$$\frac{d\xi}{dy} = \frac{3}{2}B,\ \ \frac{dR}{dy} = \frac{\xi}{R}\frac{3}{2}B. \tag{19}$$

Differentiating Equation (18) with respect to y and substituting the relations given in Equation (19) yields the Jacobian in Equation (20).

$$\left|\frac{dU}{dy}\right| = \frac{B}{2}\left[\frac{\xi/R+1}{(R+\xi)^{2/3}} + \frac{1-\xi/R}{(R-\xi)^{2/3}}\right]. \tag{20}$$

Hence, from the change in variables relation in Equation (8), the probability density function is given by

$$f_Y(y) = \phi(U(y)) \cdot \frac{B}{2}\left[\frac{\xi/R+1}{(R+\xi)^{2/3}} + \frac{1-\xi/R}{(R-\xi)^{2/3}}\right], \tag{21}$$

where $U(y)$ is given by Equation (18) and A, B, Q, ξ, R are defined in Equations (15)–(17). For a non-standardised variable X,

$$y = \frac{x-\mu}{\sigma\, k_t}, f_X(x) = \frac{1}{\sigma\, k_t} f_Y\left(\frac{x-\mu}{\sigma\, k_t}\right). \tag{22}$$

Equations (18)–(22) therefore provide the exact Hermite PDF for $\alpha_4 > 3$, without truncation of higher-order terms. The use of principal real cube roots in Equation (18) is justified by the condition $R \pm \xi \geq 0$, which ensures continuity of $U(y)$ across $\xi = 0$.

3.3. Properties and Admissible Sets

This section summarises the conditions under which the Hermite PDF, derived in the previous sections, behaves well numerically and accurately reproduces the prescribed moments. The guidance is expressed in the native parameters α_3 and α_4 through the calibrated quantities $\widetilde{h}_3$, $\widetilde{h}_4$and k_t defined above.

3.3.1. Non-Negativity and Monotonicity

The lower-branch density in Equation (13) is a first-order change-of-variables approximation; neglected terms are of order $O(\widetilde{h}^2)$. Moment matching is therefore only first-order accurate while $\left|\widetilde{h}_3\right|, \left|\widetilde{h}_4\right| \ll 1$. Using the calibrations of Equation (6), large values of $|\alpha_3|$ or $|\alpha_4 - 3|$ push the approximation outside its linear regime and bias the empirical moments by terms of order $O(\widetilde{h}^2)$.

Positivity of the first-order form in Equation (13) holds as long as the bracket term remains non-negative over the range of interest. The bracket in Equation (11) is

$$g(y) = 1 - 2\widetilde{h}_3 y - 3\widetilde{h}_4\left(y^2 - 1\right) = \left(1 + 3\widetilde{h}_4\right) - 2\widetilde{h}_3 y - 3\widetilde{h}_4 y^2. \tag{23}$$

For platykurtic cases $\widetilde{h}_4 < 0$, the corresponding parabola opens upward, and its minimum occurs at

$$y_{\min} = -\frac{\widetilde{h}_3}{3\widetilde{h}_4}, \quad g_{\min} = 1 + 3\widetilde{h}_4 + \frac{\widetilde{h}_3^2}{3\widetilde{h}_4}. \tag{24}$$

A sufficient condition for $|dU/dy| \propto g(y) > 0$ over the effective range is therefore

$$\widetilde{h}_3^2 < -3\widetilde{h}_4\left(1 + 3\widetilde{h}_4\right),\ \alpha_4 \leq 3. \tag{25}$$

When $\left|\widetilde{h}_4\right| \ll 1$, Equation (25) reduces to a transparent rule of thumb,

$$\alpha_3^2 \lesssim\ 4.5(3 - \alpha_4),\ \alpha_4 \leq 3, \tag{26}$$

obtained by substituting $\widetilde{h}_3 \simeq h_3 = \alpha_3/6$ and $\widetilde{h}_4 \simeq h_4 = (\alpha_4 - 3)/24$. Equation (26) follows by expanding Equation (25) as $\widetilde{h}_3^2 < -3\widetilde{h}_4 - 9\widetilde{h}_4^2$, neglecting the $O(\widetilde{h}_4^2)$ term for $\left|\widetilde{h}_4\right| << 1$.

Equation (26) provides a practical engineering approximation valid near the Gaussian limit, whereas Equation (25) represents the exact admissibility boundary and should be used for larger deviations in skewness or kurtosis.

Figure 2 illustrates the admissible (green) and non-admissible (purple) combinations of (α_3, α_4) implied by Equations (25)–(27), with panel (b) comparing the exact and approximate lower-branch boundaries.

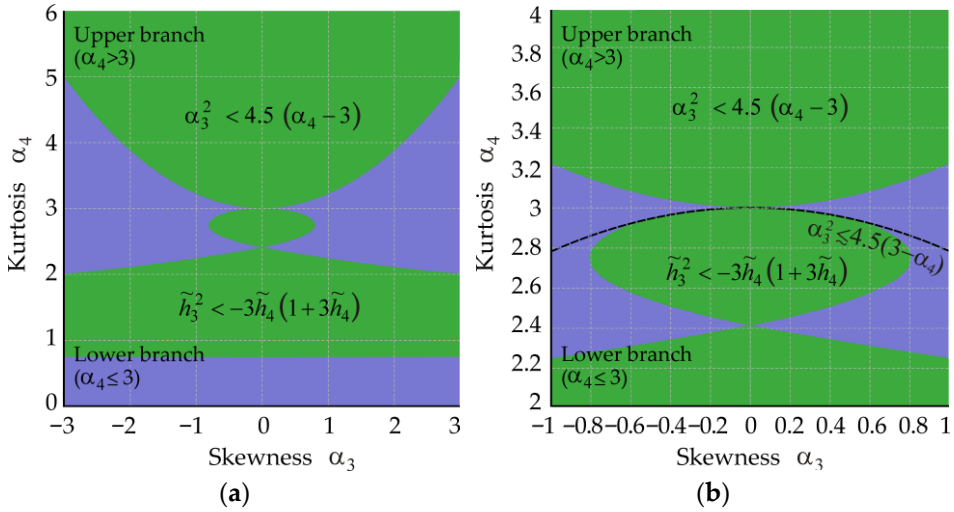

Figure 2. Admissible regions of skewness–kurtosis pairs (α_3, α_4) for the Hermite density: (**a**) Global admissibility map showing the domains in which the lower-branch criterion in Equation (25) and the upper-branch condition in Equation (27) are satisfied (green), whereas violation of either condition results in non-admissible PDFs (purple); (**b**) A zoomed view around $\alpha_4 \approx 3$ comparing the exact lower-branch boundary (Equation (25), green) with the engineering approximation given by Equation (26) (black dashed curve). The approximation is valid near the Gaussian limit but diverges for larger departures from it.

Violation of Equations (25) and (26) identifies regions where $g(y) < 0$. In exact theory, this would create negative lobes of f_Y in the far tails. In numerical implementations, such tails are often clipped to zero, which reduces the total mass $\int f_Y$ and shifts the empirical moments.

In practice, for a given pair α_3, α_4, the recommended procedure is to compute $\widetilde{h}_3$ and $\widetilde{h}_4$ and test Equation (25). If it is marginally violated, $g(y) \geq 0$ should also be verified over the effective range of $|y|$. Failure of either test indicates that the first-order model may require post-normalisation (which perturbs moments) or the adoption of a different PDF.

For $\alpha_4 > 3$, the upper-branch density defined by Equations (21) and (22) is exact, employing the Cardano real root of the depressed cubic (16). The Jacobian factor (20) follows by direct differentiation, with no truncation error. Two numerical aspects merit attention.

First, monotonicity of the mapping $U \mapsto Y$ is guaranteed while the cubic has a single real branch. In terms of α_3 and α_4, this corresponds to the classic engineering criterion

$$\alpha_3^2 \lesssim 4.5(\alpha_4 - 3), \ \alpha_4 > 3, \tag{27}$$

beyond which the cubic becomes multi-valued and the Cardano transformation no longer defines a valid PDF.

Second, although Equation (20) remains finite for all admissible parameters (since $R \pm \xi \geq 0$), near $R \approx \xi \geq 0$ the individual factors $(R \pm \xi)^{2/3}$ can become large. The balanced product in Equation (20),

$$\frac{B}{2}\left[\frac{\xi/R+1}{(R+\xi)^{2/3}} + \frac{1-\xi/R}{(R-\xi)^{2/3}}\right], \tag{28}$$

avoids catastrophic cancellation and ensures numerical stability on implementation.

3.3.2. Realised Moments

This section presents the closed-form expressions for the realised first four moments of the Hermite PDF. The inputs may be specified either through the native parameters $\theta = (\mu, \sigma, \alpha_3, \alpha_4)$ or, on the upper branch, they can also be given as target moments $M(\theta) = (\mu^*, \sigma^*, \alpha_3^*, \alpha_4^*)$. The quantity θ denotes the nominal (user-prescribed) moments, whereas $M(\theta)$ represents the moments produced by the calibrated Hermite PDF.

For $\alpha_4 > 3$ (upper branch), the variance rescaling in Equation (14) ensures exact centring and unit variance due to the orthogonality of the Hermite basis,

$$E(Y) = 0, \quad V(Y) = 1. \tag{29}$$

Consequently,

$$\mu^* = \mu, \ \ \sigma^* = \sigma. \tag{30}$$

Because Y is polynomial in the Gaussian variable U, the realised skewness and kurtosis are obtained in closed form as functions of $(\widetilde{h}_3, \widetilde{h}_4)$. These expressions are exact for the upper branch. Denoting $\widetilde{h}_3$ and $\widetilde{h}_4$ as defined in Equations (6) and (14), the realised skewness and kurtosis are given by

$$\alpha_3^* = \frac{2\widetilde{h}_3\left(4\widetilde{h}_3^2 + 54\widetilde{h}_4^2 + 18\widetilde{h}_4 + 3\right)}{\left(1 + 2\widetilde{h}_3^2 + 6\widetilde{h}_4^2\right)^{3/2}}, \tag{31}$$

$$\alpha_4^* = \frac{60\widetilde{h}_3^4 + 2232\widetilde{h}_3^2\widetilde{h}_4^2 + 576\widetilde{h}_3^2\widetilde{h}_4 + 60\widetilde{h}_3^2 + 3348\widetilde{h}_4^4 + 1296\widetilde{h}_4^3 + 252\widetilde{h}_4^2 + 24\widetilde{h}_4 + 3}{\left(1 + 2\widetilde{h}_3^2 + 6\widetilde{h}_4^2\right)^2}. \tag{32}$$

On the upper branch ($\alpha_4 > 3$), Equations (31) and (32) can be inverted to obtain $\widetilde{h}_3$ and $\widetilde{h}_4$ for prescribed (α_3^*, α_4^*). Substituting these values into Equation (14) gives the corresponding variance-scaling factor k_t, and hence a Hermite PDF with the specified target moments. It can be noted that similar explicit relations between higher-order moments and distribution parameters have recently been derived for the Weibull PDF and used to compute design quantiles in hydrological design [59].

On the lower branch ($\alpha_4 \leq 3$), the Winterstein calibration in Equation (6), combined with the first-order Neumann inversion and the change in variables in Equation (13), yields an approximate density. In this regime, only first-order preservation of the first two moments is achieved,

$$E(Y) \approx 0, \quad V(Y) \approx 1. \tag{33}$$

Consequently,

$$\mu^* = \mu + O\left(\varepsilon^2\right), \ \ (\sigma^*)^2 = \sigma^2\left[1 + O\left(\varepsilon^2\right)\right], \ \ \varepsilon = \max\left\{\left|\widetilde{h}_3\right|, \left|\widetilde{h}_4\right|\right\}. \tag{34}$$

Using Equations (31) and (32) with the lower-branch values of $(\widetilde{h}_3, \widetilde{h}_4)$ yields (α_3^*, α_4^*) to first-order; higher-order deviations increase with $|\alpha 3|$ and $|\alpha 4 - 3|$. Practical admissibility and non-negativity on the lower branch are governed by Equations (23)–(26), with the serviceability rule given by Equation (26).

Let

$$M(\theta) = (\mu^*,\ \sigma^*,\ \alpha_3^*,\ \alpha_4^*) \tag{35}$$

denote the realised moments computed from the resulting density $f_X(\cdot|\theta)$.

On the lower branch ($\alpha_4 \leq 3$), defined by the calibration in Equation (6), the mapping is only first-order accurate, and higher-order deviations increase with $|\alpha_3|$ and $|\alpha_4 - 3|$. The truncation error inherent in this approximation is quantified in Figure 3, which reports absolute deviations in the realised skewness α_3^* and kurtosis α_4^* obtained by numerical integration of the PDF.

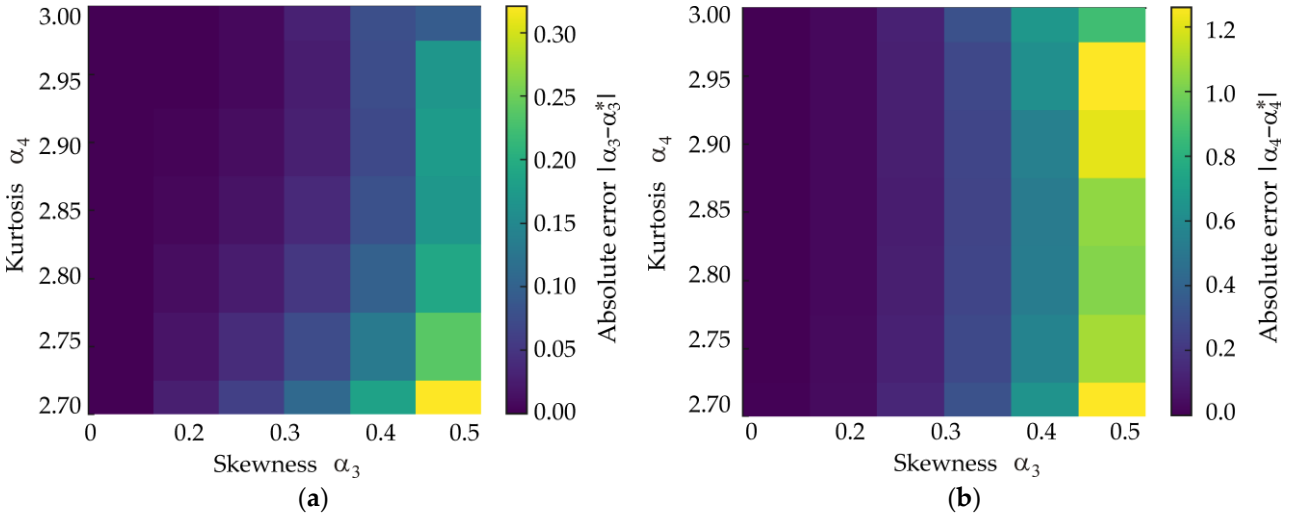

Figure 3. Truncation error of the lower-branch ($\alpha 4 \leq 3$) approximation for selected skewness–kurtosis inputs of the Hermite density: (**a**) Absolute deviation in realised skewness, $|\alpha_3 - \alpha_3^*|$; (**b**) Absolute deviation in realised kurtosis, $|\alpha_4 - \alpha_4^*|$.

On the upper branch ($\alpha_4 > 3$), the density defined by Equations (21) and (22) is exact. When the parameters $(\widetilde{h}_3, \widetilde{h}_4)$ are obtained by inverting Equations (31) and (32) for prescribed targets (α_3^*, α_4^*), numerical integration confirms that the resulting Hermite density reproduces the target skewness and kurtosis without truncation error. Small deviations may occur if the forward calibration in Equation (14) is used, reflecting its first-order character; however, these deviations vanish under inverse calibration.

For reporting purposes, the moments obtained from Equations (31) and (32) should be regarded as the reference values, while those computed by numerical integration of the lower-branch PDF may serve as a first-order consistency check.

3.4. Implementation and Workflow

Equations (25)–(28) provide analytical criteria that define the admissible regions in α_3 and α_4, ensuring both positivity and monotonicity of the Hermite PDF. For practical applications, these conditions must be embedded within an implementable computational routine. The Pascal/Delphi function presented below encodes both branches of the density, using the Winterstein calibration (Equation (6)) for $\alpha_4 \leq 3$ and the exact Cardano inversion (Equations (18)–(22)) for $\alpha_4 > 3$. The Jacobian factor is implemented in the balanced form given by Equation (28), which prevents numerical cancellation errors in the vicinity of $R \approx \xi$.

The structure of the routine reflects the admissibility conditions. When $\alpha_4 \leq 3$, the Neumann inversion is truncated at first order, consistent with the approximation in Equation (13). When $\alpha_4 > 3$, the exact cubic root is employed, and validity requires compliance with the monotonicity criterion of Equation (27). In both branches, the Gaussian kernel $\phi(U)$ is evaluated once, and rescaling by k_t ensures unit variance. A defensive clamp at

the end of the routine enforces non-negativity of the PDF and prevents spurious negative values under extreme input conditions.

The Pascal (Delphi 6) implementation of the Hermite PDF is provided in Appendix B.

This implementation enables the direct numerical evaluation of the Hermite PDF without further algebraic manipulation. In practical applications, the computational workflow proceeds as follows:

1. Compute $\widetilde{h}_3$, $\widetilde{h}_4$ and k_t from α_3 and α_4.
2. Select the branch: apply the Winterstein correction for $\alpha_4 \leq 3$, or the Cardano inversion for $\alpha_4 > 3$.
3. Verify the admissibility conditions, Equation (25) for the lower branch or Equation (27) for the upper branch.
4. Evaluate the density using the function above.
5. If the admissibility conditions are violated, the Hermite PDF cannot be used directly. In such cases, an alternative parametric or non-parametric model, which is better suited to the empirical histogram, must be adopted.

4. Fitting and Validation on Materials Data

Recent experimental studies on reinforcing steel bars, welded joints and cementitious composites report non-Gaussian measurement profiles characterised by non-negligible skewness and excess kurtosis [60,61]. As a result, strength and geometric characteristics are often modelled using Weibull, lognormal or gamma distributions [62–65]. In fibre-reinforced polymer rods and in fibre-reinforced concrete exposed to high temperatures, Weibull fits effectively capture right-skewed tails and summarise the design-relevant variability [62,63]. For metakaolin masonry blocks and large regional datasets of green concrete, lognormal or gamma laws frequently provide the best or at least competitive fits [64,65]. In rolled steels and butt-welded seams, empirical skewness and kurtosis often deviate substantially from the normal benchmark, with several cases exhibiting kurtosis greater than three, motivating the explicit use of non-Gaussian modelling [26,60,61].

For many experimental datasets, the Hermite PDF can serve as an extension of the Gaussian model that accommodates small but non-zero skewness and variable excess kurtosis. For example, in weld-toe geometry and reinforcement-height distributions that remain close to symmetric yet exhibit mild excess kurtosis, a moment-matched Hermite fit can be applied instead of switching to lognormal or gamma families [60]. For reinforcing steel, where the sign of skewness varies across production lots, both positive and negative skewness can be represented within a single parametric family while preserving the observed variance and kurtosis [26]. For regional concrete datasets that are approximately normal, small departures from symmetry and tail weight can be captured using a parsimonious Hermite approximation that retains the Gaussian baseline for interpretability [65].

In the following section, Hermite PDFs are fitted to our experimentally obtained material characteristics of structural steel [66,67], which exhibit non-Gaussian skewness and kurtosis. The fits are validated using histograms and moment analysis.

4.1. S235 Yield Strength (Lower Branch)

In engineering practice, histograms of measured quantities may deviate, to varying degrees, from the Gaussian PDF. An illustrative example is provided by the yield strength f_y of structural steel grade S235 [66]. The dataset in [66] is used to illustrate how the admissibility conditions and the PDF validation checks are applied to measured yield strength histograms. Based on n = 562 valid observations of f_y, the sample statistics were estimated as mean of 297.3 MPa, standard deviation of 16.8 MPa, skewness of 0.325, and kurtosis of 2.5415 [66].

For a platykurtic input, the lower-branch relations given by Equations (6)–(13) apply. The rule in Equation (26) gives $\alpha_3^2 \ll 4.5(3 - \alpha_4)$, and the non-negativity check based on Equations (23)–(25) is satisfied across the effective range; hence, admissibility is confirmed.

When the PDF is evaluated using the input θ = (297.3 MPa, 16.8 MPa, 0.325, 2.541), the realised moments of the resulting Hermite PDF are $M(\theta)$ = (297.429 MPa, 16.207 MPa, 0.904, 3.821), where numerical integration was performed over the range $[\mu - 19\sigma, \mu + 19\sigma]$. The Kolmogorov–Smirnov (KS) test indicates a lack of fit with $p = 0.00148 < 0.05$; see the red curve in Figure 4. This behaviour is consistent with the first-order character of Equations (9)–(13).

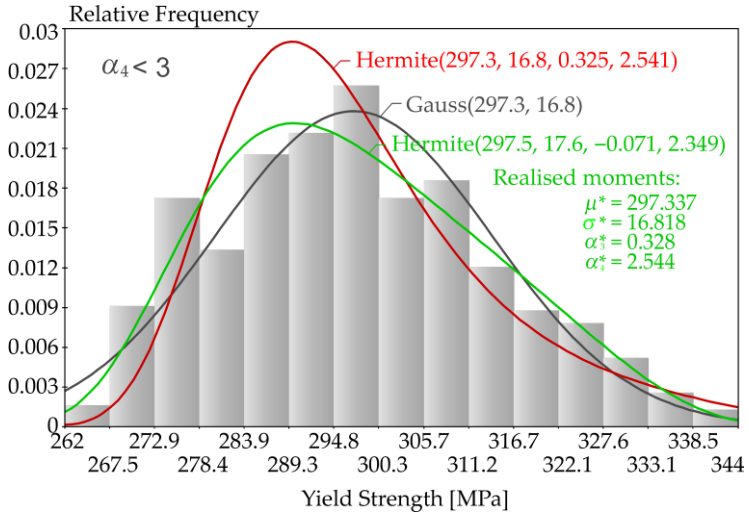

Figure 4. Hermite fit to histograms: Histogram of yield strength with Gaussian baseline and Hermite fits: direct insertion of sample moments (red; rejected by KS) and refined inputs achieving moment matching (green; not rejected).

After a minor parameter refinement within the admissible region, θ = (297.5 MPa, 17.6 MPa, −0.071, 2.349) produces realised moments $M(\theta)$ = (297.337 MPa, 16.818 MPa, 0.328, 2.544), which closely approximate the sample moments. The refinement was carried out by a local grid search over θ within the admissible region, using small parameter increments and selecting the θ that minimised the mismatch between the realised moments $M(\theta)$ and the sample moments. The KS test then reports $p = 0.2965 > 0.05$; see the green curve in Figure 4. Both parametrisations satisfy Equation (26) and the positivity condition in Equation (25). The improved fit results from compensating for the first-order truncation error inherent in Equations (9)–(13).

It can be noted that this refinement is a data-driven adjustment that compensates for the first-order truncation error of the lower-branch PDF. Therefore, θ is treated as a set of calibration parameters chosen such that the realised moments $M(\theta)$ match the sample moments. The parametrisation is therefore not intended to be exactly moment-preserving.

This structure ensures that the first four moments are taken into account while maintaining conceptual transparency. If the admissibility conditions are violated, the recommended fallback is to revert to the Gaussian PDF or to adopt an alternative model.

4.2. S235 Ductility (Upper Branch)

Ductility measurements for S235 steel, based on $n = 562$ observations, are analysed. The sample moments are $\mu = 37.8\%$, $\sigma = 2.9\%$, $\alpha_3 = -0.753$ and $\alpha_4 = 5.18$. Since $\alpha_4 > 3$, the upper-branch formulation is applicable: calibration follows Equation (14), the exact cubic inversion is performed using Equations (18)–(22), and the Jacobian is evaluated in the balanced form given by Equation (28). The monotonicity requirement specified in Equation (27) is satisfied.

Using the sample moments directly as inputs $\theta = (37.8, 2.9, -0.753, 5.18)$ (red curve in Figure 5) yields the realised moments $M(\theta) = (37.8, 2.9, -0.751, 6.026)$ when evaluated either by numerical integration over the range $[\mu - 19\sigma, \mu + 19\sigma]$ or by direct substitution into Equations (31) and (32). The discrepancy $(\alpha_3^*, \alpha_4^*) \neq (\alpha_3, \alpha_4)$ reflects the first-order nature of the polynomial translation in Equation (4). The KS test gives $p = 0.0273 < 0.05$; hence, the model is rejected.

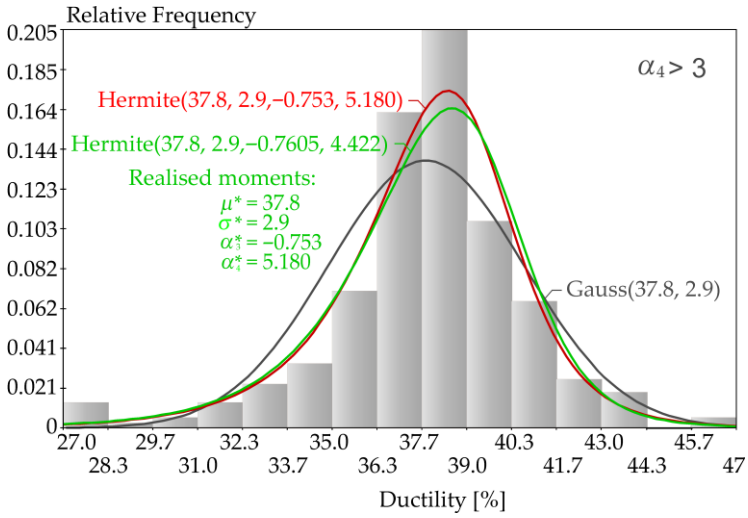

Figure 5. Hermite fit to histograms: Histogram of ductility with Gaussian baseline and Hermite fits.

A short refinement of the input parameters improves agreement between the realised and sample moments. With $\theta = (37.8, 2.9, -0.7605, 4.422)$ (green curve in Figure 5), the realised moments become $M(\theta) = (37.8, 2.9, -0.753, 5.180)$, which are very close to the sample moments. However, the KS test still rejects the model at the 5% significance level.

It can be noted that increasing the input kurtosis parameter to $\alpha_4 = 7.0$ while keeping $\mu \approx 37.8$, $\sigma \approx 2.9$ and $\alpha_3 \approx -0.762$ yields $p = 0.121 > 0.05$, i.e., non-rejection, but at the expense of a substantial deviation from the sample kurtosis. Such high kurtosis values are not unrealistic and may arise in broadly aggregated datasets, particularly when a wide range of plate thicknesses is included and the data originate from multiple producers [68].

A practical trade-off is implied: enforcing exact moment matching does not necessarily maximise agreement under the KS criterion. Notably, in all configurations considered, the Hermite fits were not rejected by the Anderson–Darling (AD) goodness-of-fit test, indicating adequate tail behaviour despite the KS test's sensitivity to central discrepancies for large n.

The different outcomes of the KS and AD tests are not contradictory. The KS statistic measures the maximum deviation between the empirical and fitted distribution functions over the full range. For a sample size of $n = 562$, even small systematic discrepancies in the central part of the distribution can lead to rejection at the 5% level. In contrast, the AD test places greater weight on the tails. It is therefore possible to observe KS rejection together with AD non-rejection when the fitted model captures tail behaviour adequately, while small deviations remain in the central region.

4.3. Extreme-Moment Inputs

This subsection examines inputs $\theta = (\mu, \sigma, \alpha_3, \alpha_4)$ that lie outside the perturbative regime assumed in the derivation. In such cases, θ must be regarded as control parameters of the transformation rather than as guaranteed realised moments, and the resulting PDF $f_X(\cdot|\theta)$ must be validated a posteriori. Validation includes checks for non-negativity and normalisation, admissibility via Equation (25) for the lower branch and Equation (27)

for the upper branch, and consistency of the realised moments $M(\theta) = (\mu^*, \sigma^*, \alpha_3^*, \alpha_4^*)$ with the intended targets. Where discrepancies occur, a constrained numerical calibration of θ is required, followed by re-evaluation using Equation (13) for the lower branch or Equations (21) and (22) for the upper branch, with the balanced Jacobian defined in Equation (28).

For strongly platykurtic inputs ($\alpha_4 < 3$), the first-order representation of the lower branch, $f_Y(y) \approx \phi(U(y))\ g(y)$ with $g(y) = 1 - 2\widetilde{h}_3 y - 3\widetilde{h}_4(y^2 - 1)$ defined by Equations (11) and (23), governs admissibility and the shape of the PDF. When $\widetilde{h}_4 < 0$, the factor $g(y)$ forms a convex parabola whose minimum occurs at $y_{\min}$ and reaches $g_{\min}$ as given in Equation (24). Positivity requires $g_{\min} > 0$, corresponding to the bound in Equation (25). This bound explains two features observed in Figure 6. Firstly, very small target kurtosis depresses the centre of $g(y)$ and may create a double-humped PDF even when the mapping remains monotonic. Secondly, large values of $|\alpha 3|$ shift the minimum of $g(y)$ and tighten the constraint imposed by Equation (25).

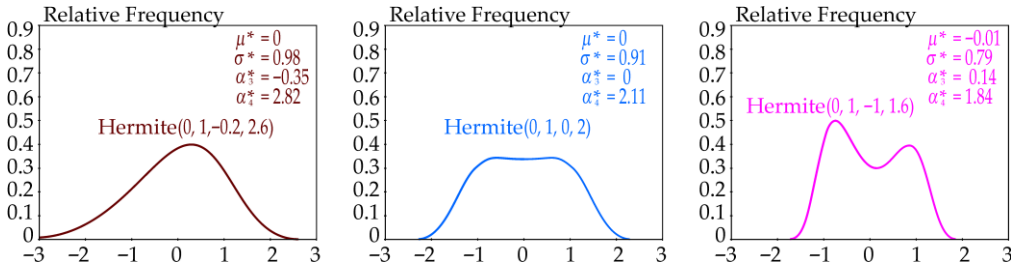

Figure 6. Platykurtic branch ($\alpha_4 < 3$): illustrative Hermite PDFs under extreme-moment inputs.

In Figure 6, the emergence of double-humped shapes follows directly from the quadratic factor $g(y)$ in Equation (23). For $\widetilde{h}_4 < 0$, $g(y)$ reduces the central weight relative to larger values of y, and increasing $|\alpha_3|$ shifts the location of its minimum. This behaviour explains both the observed asymmetry and the tightening of the non-negativity constraint in Equation (25).

For leptokurtic inputs ($\alpha_4 > 3$), the upper branch employs the exact cubic inversion defined by Equations (18)–(22), and monotonicity reduces to the single inequality expressed in Equation (27). Because the right-hand side of Equation (27) increases with $\alpha_4 - 3$, larger magnitudes of $|\alpha_3|$ become admissible as kurtosis increases. This behaviour is consistent with the broader family of attainable PDF shapes illustrated in Figure 7. The Jacobian remains finite when evaluated using the balanced product form in Equation (28). Nevertheless, even on this branch, the polynomial translation given in Equation (4) represents a cubic truncation. Consequently, the realised higher-order moments deviate from the input values once (α_3, α_4) move sufficiently far from (0, 3).

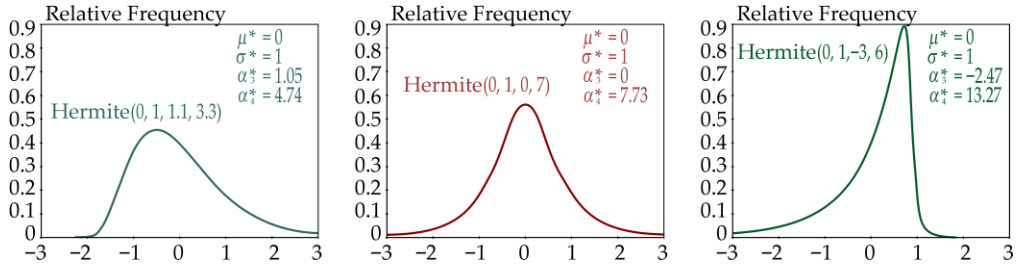

Figure 7. Leptokurtic branch ($\alpha_4 > 3$): illustrative Hermite PDFs under extreme-moment inputs.

In Figure 7, heavier tails and stronger asymmetry arise because increasing α_4 relaxes the monotonicity bound in Equation (27), thereby admitting larger values of $|\alpha_3|$. Under these settings, the exact cubic inversion typically yields a more pronounced tail stretching.

In practical modelling, the extreme-input regime can generate useful PDF shapes, including light-tailed or bimodal forms. The reliability of such fits depends on enforcing the admissibility conditions given by Equations (25)–(27), verifying the normalisation and non-negativity of f_X, and, where necessary, numerically calibrating θ so that $M(\theta)$ satisfies the desired moment constraints while the PDF remains admissible.

Figure 8 summarises the practical usability of the Hermite PDF in the (α_3, α_4) plane for $\mu = 0$ and $\sigma = 1$, based on numerical integration over the interval $[-18, 18]$. Figure 8 complements the analytical admissibility conditions in Equations (25) and (27) by showing the numerical behaviour of the implemented PDF under finite-range integration.

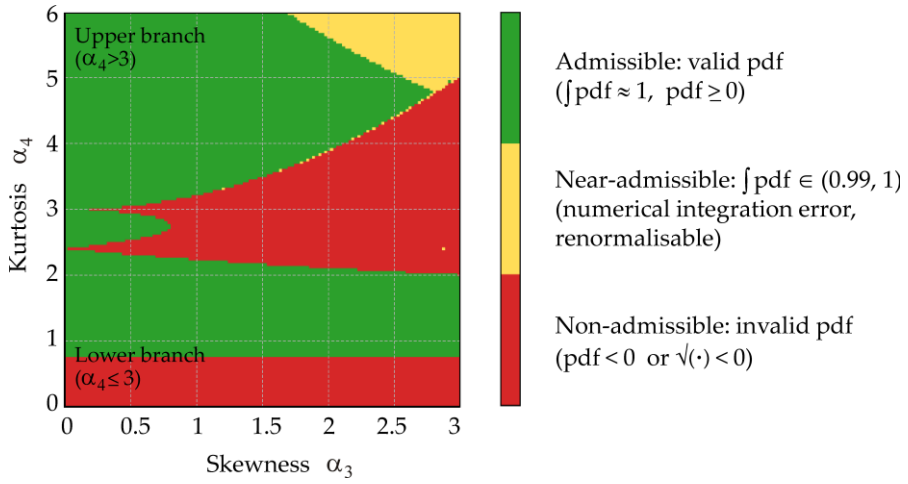

Figure 8. Practical usability map of the Hermite PDF in the (α_3, α_4) plane for $\mu = 0$ and $\sigma = 1$, based on numerical integration over the interval $[-18, 18]$. Green indicates an admissible PDF with normalisation close to unity and non-negativity satisfied. Yellow indicates a small mass deficit caused by numerical integration, which decreases as the integration is refined and can be removed by renormalisation. Red indicates a non-admissible PDF due to negativity or non-real terms, see Appendix B. The red region corresponds to the non-admissible domain shown in purple in Figure 2.

The model cannot be used once (α_3, α_4) approaches or enters the non-admissible (red) region, where the density violates non-negativity or becomes non-real, see Appendix B. In the near-admissible (yellow) region, the deviation from unity manifests as a small deficit of the PDF integral that depends on the numerical integration settings. The yellow region contracts when the integration is refined or when the integration interval is extended, and it is primarily observed in the upper right-corner, where heavier tails are present.

5. Reliability Application

In EN 1990, design values are obtained from the mean and standard deviation using the FORM [1]. When full probability distributions are specified, design quantiles are typically derived from Gaussian, lognormal or Gumbel laws [1]. A review of the literature reveals no published calculation of the 0.12% quantile directly under a Hermite probability density function. Existing applications of the Hermite model have focused primarily on peak factor estimation [37], dynamic reliability [51], and fatigue assessment [53], rather than on code-level design quantile evaluation. Motivated by these gaps, the following section derives closed-form design quantiles under a Hermite density, allowing skewness and kurtosis to be incorporated consistently into the estimation of design quantiles.

5.1. Design Quantiles

5.1.1. EN 1990 Quantile

Let the structural resistance R and the load effect F be modelled as independent random variables with means μ_R, μ_F and standard deviations σ_R, σ_F, see, e.g., [69]. The performance function is defined as

$$Z = R - F. \tag{36}$$

Under the Gaussian baseline, the reliability index

$$\beta = \frac{\mu_Z}{\sigma_Z}, \ \ \mu_Z = \mu_R - \mu_F, \ \ \sigma_Z = \sqrt{\sigma_R^2 + \sigma_F^2}, \tag{37}$$

leads to the failure probability $P_f = \Phi(-\beta)$. A recent review discusses the underlying target reliability concepts and summarises typical target reliability index values β values adopted across contemporary design standards, see [70]. Eurocode practice compares β with a target reliability index β_d (for the ultimate limit state: $\beta_d \approx 3.8$, corresponding to $P_f \approx 7.2 \times 10^{-5}$).

Within FORM, the contribution of R and F to σ_Z is described by sensitivity factors α_R, $\alpha_F > 0$ (for independent normal variables $\alpha_R = \sigma_R/\sigma_Z$, $\alpha_F = \sigma_F/\sigma_Z$, some standards adopt fixed values, e.g., $\alpha_R = 0.8$, $\alpha_F = 0.7$ [1]). The design values are then expressed as

$$R_{d,FORM} = \mu_R - \alpha_R \beta_d \sigma_R, \tag{38}$$

$$F_{d,FORM} = \mu_F + \alpha_F \beta_d \sigma_F. \tag{39}$$

The reliability requirement is verified through the inequality of the design quantiles:

$$F_{d,FORM} \leq R_d R_{d,FORM}. \tag{40}$$

The design resistance $R_{d,FORM}$ represents the lower Gaussian quantile at probability level

$$p_d = \Phi(-\alpha_R \beta_d), \tag{41}$$

where, for the ultimate limit state, $\beta_d = 3.8$ and $\alpha_R = 0.8$ are used for reliability class RC2 in [1]. This gives $p_d \approx \Phi(-3.04) \approx 0.0012$.

The design load action $F_{d,FORM}$ corresponds to the higher Gaussian quantile at probability level

$$p_F = \Phi(+\alpha_F \beta_d), \tag{42}$$

where $\beta_d = 3.8$ and $\alpha_F = 0.7$ are used for RC2 [1], giving $p_d \approx \Phi(+2.66) \approx 0.996$.

Symbols α_3, α_4 denote skewness and kurtosis used in the Hermite PDF, while α_R and α_F are FORM sensitivity coefficients (weight factors) and must not be confused.

In practice, the EN 1990 FORM quantile can be retained as a baseline check, while the Hermite quantile is evaluated at the same target probability level when skewness and kurtosis are available. The resulting design resistance is then verified using the standard EN 1990 inequality in exactly the same manner, and the Hermite fit should be accepted only after the admissibility, normalisation, and non-negativity checks have been satisfied.

5.1.2. Hermite Quantile (Closed Form)

Let $U \sim N(0, 1)$ and define the Hermite translation as

$$T(U) = k_t]U + \widetilde{h}_3\left(U^2 - 1\right) + \widetilde{h}_4\left(U^3 - 3U\right) [;, \tag{43}$$

with branch-specific $\widetilde{h}_3$, $\widetilde{h}_4$ and k_t determined by ($\alpha_{3,R}$, $\alpha_{4,R}$) under the admissibility and monotonicity conditions stated earlier. The structural resistance is then

$$R = \mu_R + \sigma_R T(U). \tag{44}$$

If T is strictly increasing (upper branch: exact, lower branch: valid in the small-departure regime), the cumulative density function (CDF) transforms as $F_R(r) = \Phi(U(r))$. Hence, the p-quantile is obtained by inserting the Gaussian p-quantile $z_p = \Phi^{-1}(p)$ into the forward map:

$$q_p = \mu_R + \sigma_R\, k_t \left[z_p + \widetilde{h}_3 \left(z_p^2 - 1 \right) + \widetilde{h}_4 \left(z_p^3 - 3z_p \right) \right]., \tag{45}$$

where $z_p = \Phi^{-1}(p)$. For design purposes in the FORM sense, retain the target probability content

$$p_d = \Phi(-\alpha_R \beta_d), \quad z_d = -\alpha_R \beta_d, \tag{46}$$

In EN 1990 [1], FORM design values correspond to a fixed target quantile level determined by the target reliability index β_d and the sensitivity factor α_R, see Equation (46). Equation (47) preserves the same target level but evaluates the quantile under the Hermite model through the translation T, thereby accounting for non-Gaussian skewness and kurtosis. The Hermite-based design resistance is defined as:

$$R_{d,HERM} = \mu_R + \sigma_R\, k_t \left[z_d + \widetilde{h}_3 \left(z_d^2 - 1 \right) + \widetilde{h}_4 \left(z_d^3 - 3z_d \right) \right]. \tag{47}$$

This expression reduces to the Gaussian design value $R_{d,FORM} = \mu_R - \alpha_R \beta_d \sigma_R$ in the limit $\alpha_{3,R} \to 0$, $\alpha_{4,R} \to 3$, where $\widetilde{h}_3$, $\widetilde{h}_4 \to 0$ and $k_t \to 1$. Examples of design quantiles for normalised distributions with $\mu_R = 1$ $\sigma_R = 1$ are shown in Figure 9.

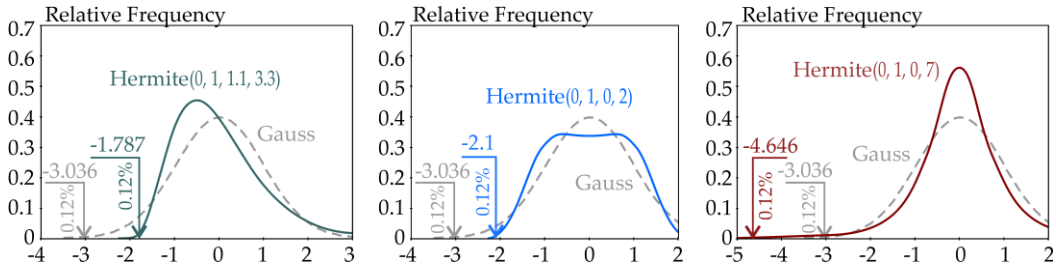

Figure 9. Comparison of design quantiles $R_{d,HERM}$ with $R_{d,FORM}$ for $\beta_d = 3.8$.

When the load effect F is modelled as non-Gaussian, the same construction applies using parameters (μ_F, σ_F, $\alpha_{3,F}$, $\alpha_{4,F}$) and coefficients $\widetilde{h}_3^{(F)}$, $\widetilde{h}_4^{(F)}$, $k_t^{(F)}$. The design quantile corresponds to $p_F = \Phi(+\alpha_F \beta_d)$ with $z_F = +\alpha_F \beta_d$, giving

$$F_{d,HERM} = \mu_F + \sigma_F\, k_t^{(F)} \left[z_F + \widetilde{h}_3^{(F)} \left(z_F^2 - 1 \right) + \widetilde{h}_4^{(F)} \left(z_F^3 - 3z_F \right) \right], \tag{48}$$

which reduces to the Gaussian $F_{d,FORM}$ as $\alpha_{3,F} \to 0$ and $\alpha_{4,F} \to 3$. In the present study, only $R_{d,HERM}$ is used in the examples.

5.2. Case Study: Pin-Jointed Tie System

A pin-connected node is supported by two axially loaded ties and subjected to a vertical gravity force $F > 0$, see Figure 10.

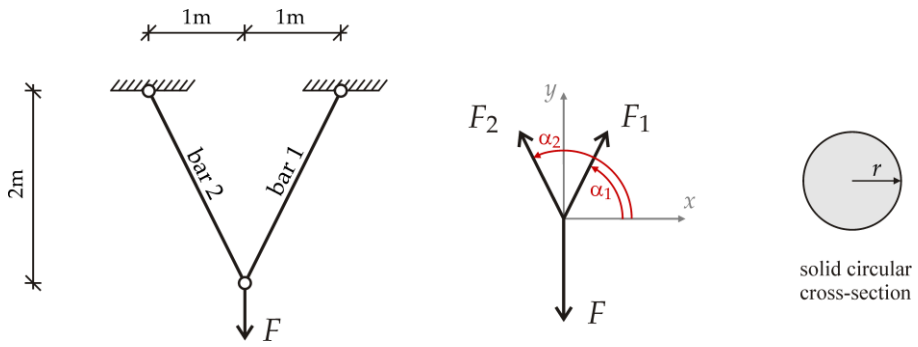

Figure 10. Two pin-jointed bars with equilibrium of the internal force magnitudes F_1 and F_2 and external load F.

Small-displacement statics and perfectly pinned joints are assumed; self-weight and bending effects are neglected. Here, F_1 and F_2 denote the magnitudes of the axial forces in bars 1 and 2. Static equilibrium of the node gives

$$\sum F_x = F_1 \cos\alpha_1 + F_2 \cos\alpha_2 = 0 \Rightarrow F_1 = F_2, \tag{49}$$

$$\sum F_y = F_1 \sin\alpha_1 + F_2 \sin\alpha_2 - F = 0 \Rightarrow F = \frac{2}{\sqrt{5}}(F_1 + F_2) = \frac{4}{\sqrt{5}}F_1, \tag{50}$$

where $\sin\alpha_1 = \sin\alpha_2 = 2/\sqrt{5}$ and $\cos\alpha_1 = -\cos\alpha_2 = 1/\sqrt{5}$. The axial force in each tie under given vertical load is $F_1 = F_2 = \sqrt{5}/4F$ by Equation (50).

Let f_{y1} and f_{y2} denote the yield strengths of the two steel ties, and A_1 and A_2 their respective cross-sectional areas. The axial load-carrying capacities are

$$N_{R1} = f_{y1}A_1,\ N_{R2} = f_{y2}A_2, \tag{51}$$

where f_y is expressed in MPa and A in mm^2, giving N_R in N. The vertical load action that brings tie i to its ultimate limit state follows from Equation (50):

$$F_{Ri} = \frac{4}{\sqrt{5}}N_{Ri}\ (i = 1,\ 2), \tag{52}$$

The structural (system) resistance is governed by the weaker tie reaching yield first:

$$R = \min\{F_{R1},\ F_{R2}\} = \frac{4}{\sqrt{5}}\min\{f_{y1}A_1,\ f_{y2}A_2\} = \frac{4\pi}{\sqrt{5}}\min\left\{f_{y1}r_1^2,\ f_{y2}r_2^2\right\}, \tag{53}$$

where $A_i = \pi r_i^2$ $(i = 1, 2)$ denotes the cross-sectional area of the solid circular bar with radius r_i. Equation (53) is nonlinear, because the system resistance is defined as the minimum of the two bar load-carrying capacities, each defined by the product of the yield strength and the squared radius. This weakest-link selection does not preserve Gaussianity and can introduce skewness even when the inputs are Gaussian.

It can be noted, that comparable nonlinear input–output relations occur in nonlinear shell analysis [71,72], in the nonlinear reliability assessment of steel frames with Gaussian imperfections [31], and in nonlinear fatigue analysis under Gaussian loading [73]. Studies [31,71,73] show that nonlinear structural models with Gaussian input variables often yield non-Gaussian outputs due to the inherent nonlinearity of the input–output relationship. Skewness, kurtosis and other higher-order features of model output may therefore arise from the model itself, from the input distributions, or from a combination of both.

5.2.1. Inputs Random Quantities

Equation (53) is a function of four random quantities, where input vector is

$$\boldsymbol{X} = \left(f_{y1},\ r_1,\ f_{y2},\ r_2\right)^T \tag{54}$$

and the model output is the structural resistance $Y = R(\boldsymbol{X})$ obtained from Equation (53). In Equation (54), the four input variables are assumed to be mutually independent, and both members are assumed to possess identical statistical distributions of material and geometric properties. This independence assumption is adopted as a simplifying baseline, since joint data required to quantify correlations between material and geometric variables are not available for the present case study.

The yield strength f_{yi} is treated as a random variable described by the histogram shown in Figure 4. The green Hermite PDF is adopted, as it reproduces the first four statistical moments of the histogram with numerical precision and passes the KS test. The mean, standard deviation, skewness, and kurtosis of this Hermite PDF are consistent with the observed sample statistics, providing a mathematically admissible representation of yield strength while preserving the probabilistic characteristics of the measured data, see Table 1.

Table 1. Input random quantities.

Quantity	μ	σ	α_3	α_4	Density
Yield strength f_{y1}	297.5	17.6	-0.071	2.349	Hermite
Radius r_1	5	0.1021	$\alpha_{3,r}$	$\alpha_{4,r}$	Hermite
Yield strength f_{y2}	297.5	17.6	-0.071	2.349	Hermite
Radius r_2	5	0.1021	$\alpha_{3,r}$	$\alpha_{4,r}$	Hermite

The skewness and kurtosis of the radius r_i are denoted by $\alpha_{3,r}$ and $\alpha_{4,r}$. The parametric study fixes $\mu_r = 5$ mm and $\sigma_r = 0.1021$ mm, while the pairs $(\alpha_{3,r}, \alpha_{4,r}) = (0, 3), (-1, 4), (-2, 5), (-3, 6)$ are examined.

The radius r_i is treated as a random variable for hot-rolled steel bars with nominal value 5 mm. When direct measurements of bar radii are unavailable, the diameter can be taken as $\mu_r = 5$ mm and the standard deviation σ_r is estimated assuming that 95 percent of realisations lie within the tolerance limits specified in EN 10060:2003 [74], which gives $\sigma_r = 0.1021$ mm. Information on skewness and kurtosis is not provided in Eurocode design or tolerance standards. A Gaussian PDF is therefore adopted for r_i as a simplified model in the absence of higher-order statistics.

Nevertheless, statistical investigations of geometric characteristics in other rolled profiles, such as IPE sections [66,67], have reported skewness values between -0.5448 and 1.0545 and kurtosis values between 2.65 and 7.473, indicating that actual distributions may deviate from the Gaussian assumption. All input random quantities are summarised in Table 1.

$\alpha_{3,r}\alpha_{4,r}\alpha_{3,r}\alpha_{4,r}$In Table 1, the skewness and kurtosis of r_i are treated as uncertain parameters and their influence on the output statistics of R is examined. From an engineering perspective, configurations with a smaller mean and a larger standard deviation of R are considered less safe. Under fixed $\mu_r = 5$ mm and $\sigma_r = 0.1021$ mm, such behaviour is promoted when the distribution of r_i exhibits negative skewness and leptokurtosis. The subsequent analyses, therefore, focus on deviations from the Gaussian baseline toward $\alpha_{3,r} < 0$, and $\alpha_{4,r} > 3$.

5.2.2. Sobol Sensitivity Analysis of Resistance

Sobol sensitivity analysis is used to assess how variations in the skewness and kurtosis of the radius r influence the variance of the model output R. In this case study, the pairs $(\alpha_{3,r}, \alpha_{4,r}) = (0, 3), (-1, 4), (-2, 5), (-3, 6)$ are considered, see Table 1.

The first-order and total Sobol indices for input X_i are defined as

$$S_i = \frac{V(E(Y|X_i))}{V(Y)},\ S_{Ti} = 1 - \frac{V(E(Y|X_{\sim i}))}{V(Y)}, \tag{55}$$

where $E(\cdot)$ denotes the mean value, $V(\cdot)$ the variance and $X_{\sim i}$ represents the full set of input variables excluding X_i.

Expectations and variance $V(Y)$ were evaluated by tensor-product midpoint quadrature on a uniform grid $[lb_j, ub_j]$ with $N = 400$ nodes per dimension. For $j = 1, \ldots, 4$ let $dx_j = (ub_j - lb_j)/N$ and $x_j(i_j) = lb_j + (i_j + 0.5)$ for $i_j = 0, \ldots, N-1$. For independent inputs, the joint density is given by $f_1(x_1)f_2(x_2)f_3(x_3)f_4(x_4)$. Then

$$E(Y) \approx \sum_{i_1=0}^{N-1}\sum_{i_2=0}^{N-1}\sum_{i_3=0}^{N-1}\sum_{i_4=0}^{N-1} Y(x_1(i_1), x_2(i_2), x_3(i_3), x_4(i_4))\prod_{j=1}^{4} f_j\left(x_j\left(i_j\right)\right)dx_1dx_2dx_3dx_4, \tag{56}$$

$$E\left(Y^2\right) \approx \sum_{i_1=0}^{N-1}\sum_{i_2=0}^{N-1}\sum_{i_3=0}^{N-1}\sum_{i_4=0}^{N-1} Y(x_1(i_1), x_2(i_2), x_3(i_3), x_4(i_{41}))^2\prod_{j=1}^{4} f_j\left(x_j\left(i_j\right)\right)dx_1dx_2dx_3dx_4, \tag{57}$$

$$V(Y) \approx E\left(Y^2\right) - E(Y)^2. \tag{58}$$

For the first-order index S_1, the conditional mean on the grid of X_1 was evaluated using triple midpoint sums over the remaining coordinates:

$$E(Y|X_1 = x_1(i_1)) \approx \sum_{i_2=0}^{N-1}\sum_{i_3=0}^{N-1}\sum_{i_4=0}^{N-1} Y(x_1(i_1), x_2(i_2), x_3(i_3), x_4(i_4))\prod_{j=2}^{3} f_j\left(x_j\left(i_j\right)\right)dx_2dx_3dx_4, \tag{59}$$

and the variance of the conditional mean and the corresponding sensitivity index were obtained as

$$V(E(Y|X_1)) \approx \sum_{i_1=0}^{N-1}(E(Y|X_1 = x_1(i_1)))^2 f_1(x_1(i_1))dx_1 - E(Y)^2,\ S_1 = \frac{V(E(Y|X_1))}{V(Y)}, \tag{60}$$

where $E(Y) = E(E(Y|X_1))$. Kahan compensated summation was applied to both unconditional and conditional sums to reduce round-off error. The interval $[lb_j, ub_j]$ was defined by $lb_j = \mu_i - (10 - \alpha_3)\,\sigma_i$ and $ub_j = \mu_i + (10 + \alpha_3)\,\sigma_i$ ensuring adequate coverage of the left tails arising from negative skewness ($\alpha_3 < 0$). The remaining first-order indices and total indices were estimated analogously.

Numerical results are presented for the radius-moment pairs $(\alpha_{3,r}, \alpha_{4,r}) = (0, 3), (-1, 4), (-2, 5), (-3, 6)$, as listed in Table 1. In Figure 11, the baseline case is depicted, where the radius r follows a Gaussian PDF with $(\alpha_{3,r}, \alpha_{4,r}) = (0, 3)$. The Gaussian PDF of r is shown in the left panel. Its effect on the variance decomposition is shown in the two right-hand panels. The pie chart presents the first-order Sobol indices S_i, with the grey sector labelled "higher order" corresponding to $1 - \sum S_i$. The bar chart displays the corresponding total indices S_{Ti}.

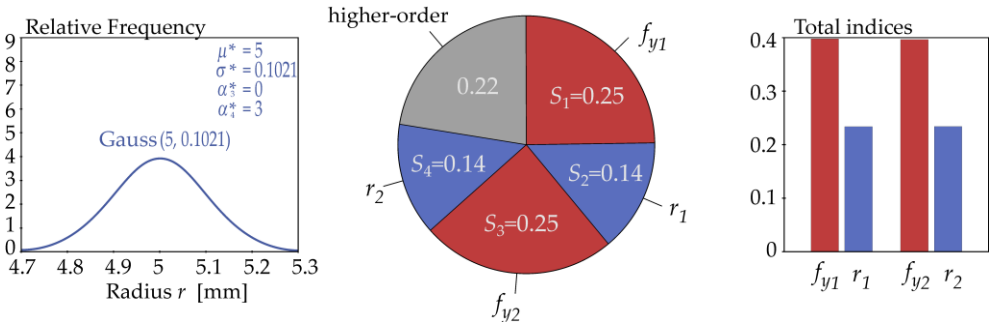

Figure 11. Gaussian density of the input radius r and Sobol first-order and total sensitivity indices of the output resistance R.

Figures 12–14 present the non-Gaussian cases. The radius r is modelled by a Hermite PDF with μ_r = 5 mm and σ_r = 0.1021 mm, using the moment pairs $(\alpha_{3,r}, \alpha_{4,r})$ = (−1, 4), (−2, 5), (−3, 6), as listed in Table 1. Figures 11–14 show, from left to right, the adopted Hermite PDF of r, the first-order Sobol indices S_i in the central panel, and the total indices S_{Ti} in the right-hand panel.

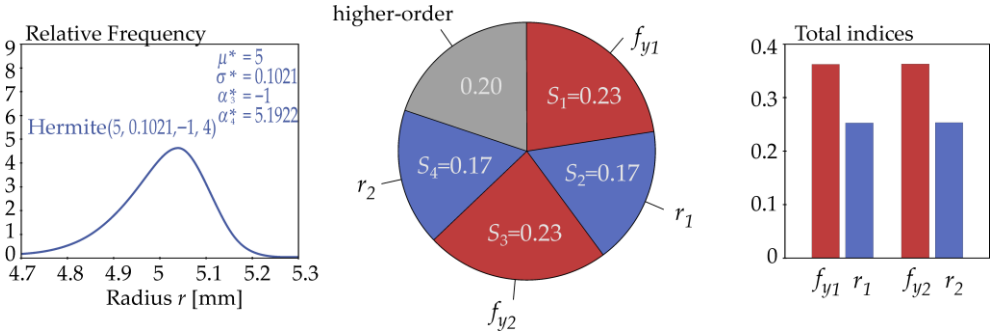

Figure 12. Hermite density of the input radius r with negative skewness and elevated kurtosis $(\alpha_{3,r}, \alpha_{4,r})$ = (−1, 4) and Sobol first-order and total sensitivity indices of the output resistance R.

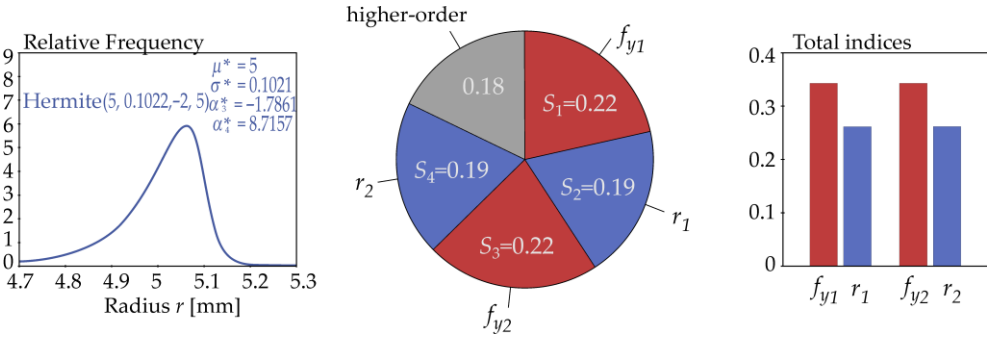

Figure 13. Hermite density of the input radius r with stronger negative skewness and higher kurtosis $(\alpha_{3,r}, \alpha_{4,r})$ = (−2, 5) and Sobol first-order and total sensitivity indices of the output resistance R.

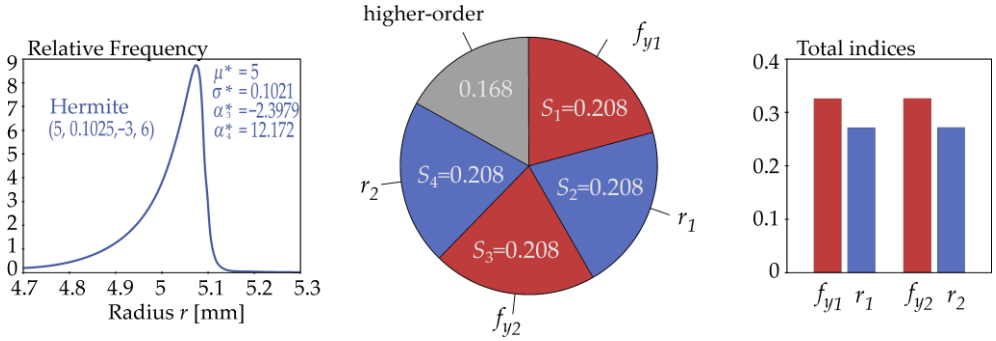

Figure 14. Hermite density of the input radius r with pronounced negative skewness and markedly higher kurtosis $(\alpha_{3,r}, \alpha_{4,r}) = (-3, 6)$ and Sobol first-order and total sensitivity indices of the output R.

The first-order Sobol indices in Figures 11–14 exhibit a symmetric pattern that reflects the symmetry of the stochastic model, see Figure 10. In the Gaussian baseline case $(\alpha_{3,r}, \alpha_{4,r}) = (0, 3)$, $S_{fy1} = S_{fy2} \approx 0.25$ and $S_{r1} = S_{r2} \approx 0.14$, with the remainder $1 - \sum_i S_i \approx 0.22$ attributed to higher-order effects. For the Hermite cases $(-1, 4)$, $(-2, 5)$, $(-3, 6)$ the indices of the radii increase monotonically to about 0.17, 0.19, and 0.21, while the indices of the yield strengths decrease to approximately 0.23, 0.22, and 0.21. The higher-order remainder decreases concurrently from about 0.20 to 0.18 and 0.17. Departures of the radius distribution toward negative skewness and leptokurtosis, therefore, increase the first-order contribution of r_1 and r_2 to $V(Y)$, accompanied by a reduction in the higher-order remainder. This follows from Equation (53), because the squared radius and the minimum operator emphasise low-radius realisations, such that occasional small radii control the system resistance and dominate its variability.

The total Sobol indices S_{Ti} in Figures 11–14 quantify the overall contribution of each input to $V(Y)$, including all interaction terms. In the Gaussian baseline case $(\alpha_{3,r}, \alpha_{4,r}) = (0, 3)$ the yield strengths dominate, while the radii have comparatively smaller total effects. As the radius distribution departs progressively from the Gaussian shape toward $(-1, 4)$, $(-2, 5)$, and $(-3, 6)$, the total effects of r_1 and r_2 increase, whereas the total effects of f_{y1} and f_{y2} decrease. In the extreme case $(-3, 6)$ the total effect of each radius approaches that of the corresponding yield strength, indicating a comparable overall influence on $V(Y)$. The differences $S_{Ti} - S_i$ show that interaction effects remain more pronounced for the yield strengths, whereas the radii gain importance primarily due to their first-order contributions.

5.2.3. Output Statistics and Design Quantiles

For the resistance R, it is essential to identify cases in which the random output exhibits higher standard deviation, as these cases are potentially more critical from a design perspective.

The results of the sensitivity analysis indicate that the standard deviation of R increases when deviations from the Gaussian distribution are accompanied by increasing kurtosis and decreasing skewness of the radius r. This variation in skewness and kurtosis of the input radius r has relatively little influence on the mean value of resistance R but a considerable effect on its standard deviation. Consequently, an increase in kurtosis combined with a decrease in skewness of the radius r leads to a higher coefficient of variation in resistance R, and therefore to a lower design resistance $R_{d,FORM}$, which is evaluated according to Equation (38), where $R_{d,FORM}$ corresponds to the target reliability index $\beta_d = 3.8$, which in turn represents a failure probability of $P_f = 7.2 \times 10^{-5}$ [1].

The input random variables are defined in Table 1. The statistical analysis of R was performed by numerical integration, following the same procedure used for the evaluation

of the first two statistical moments in the previous chapter. Table 2 reports moments obtained by numerical integration. Monte Carlo results are reported separately at the end of this section for verification. The yield strength is assumed to follow the green Hermite PDF introduced in Section 3.1, see Figure 4. The results of the statistical analysis of the output resistance R are presented in Table 2.

Table 2. Output moments of R and design value R_d for Gaussian Hermite.

Density of Input Radius r	μ_R^* [kN]	σ_R^* [kN]	$\alpha_{3,R}^*$ [-]	$\alpha_{4,R}^*$ [-]	$R_{d,FORM}$ [kN]
Gauss(5, 0.1021)	40.1431	2.2494	0.2161	3.0073	33.3048
Hermite(5, 0.1021, −1, 4)	40.1513	2.3351	−0.0784	3.6834	33.0523
Hermite(5, 0.1022, −2, 5)	40.1611	2.4039	−0.4209	5.9759	32.8532
Hermite(5, 0.1025, −3, 6)	40.1702	2.4539	−0.6874	7.8546	32.7103

μ_R^*, σ_R^*, $\alpha_{3,R}^*$, $\alpha_{4,R}^*$ denote moments of R evaluated by numerical integration with $N = 400$.

Table 2 reports the realised moments of R and the corresponding design resistance $R_{d,FORM}$ for the Gaussian baseline and for Hermite PDFs with moment pairs $(\alpha_{3,r}, \alpha_{4,r}) = (-1, 4), (-2, 5), (-3, 6)$. The mean value of R changes only marginally (by approximately +0.07%), whereas the standard deviation increases monotonically by about 9%. The output skewness shifts from positive to negative, and the output kurtosis increases markedly, indicating the development of heavier tails. This sign change occurs because the baseline output skewness is dominated by the yield strength distribution, whereas under left-skewed and leptokurtic radius distributions the squared radius term and the minimum operator emphasise small radius random realisations. Consequently, the lower tail governs the response, and the output becomes negatively skewed. As a result of this increase in the standard deviation of R, the design value $R_{d,FORM}$ decreases from 33.3048 to 32.7103 (a reduction of approximately 1.8%).

In Equation (38), the design value $R_{d,FORM}$ corresponds to the 0.12% quantile of a Gaussian PDF, as defined in EN 1990 [1]. According to [1], a Gaussian model is admissible for both loads and structural resistance. However, large skewness and kurtosis and deviations from the Gaussian PDF may make the FORM concept insufficient to ensure reliable design, see, e.g., [75].

A more accurate 0.12% quantile can be obtained by using all four statistical moments listed in the last row of Table 2. For example, for the input parameters θ = (40.17, 2.4539, −0.7, 6.93), the 0.12% quantile can be obtained by approximating R using the Hermite PDF function as 27.4154 kN, which is significantly different from the Gaussian design value $R_{d,FORM}$ = 32.7103 kN obtained from Equation (38).

Table 3 compares the design resistances $R_{d,FORM}$ obtained from Hermite PDFs and from the FORM expression in Equation (38). The first column lists the parameters (μ, σ, α_3, α_4) of the Hermite models for R, determined numerically to achieve the four moments of R given in Table 2. The second column provides the design resistance $R_{d,HERM\text{-}INT}$ evaluated as the 0.12% quantile computed by numerical integration of the Hermite PDF. The third column lists the design value $R_{d,HERM}$ calculated using Equation (47). It is evident that the values $R_{d,HERM\text{-}INT}$ and $R_{d,HERM}$ are in excellent agreement.

The fourth column reports the design value $R_{d,FORM}$ computed by the FORM, which depends solely on the mean μ and standard deviation σ. Comparison of the design values from the Hermite distribution $R_{d,HERM}$ with the corresponding $R_{d,FORM}$ value (last column) shows a significant influence of skewness and kurtosis on the design quantile. The discrepancy increases as α_3 becomes more negative and α_4 increases.

Table 3. Comparison of design quantiles of resistance R: Hermite closed form ($R_{d,HERM}$), numerical integration ($R_{d,HERM\text{-}INT}$), and FORM ($R_{d,FORM}$).

Density of Output Resistance R	$R_{d,HERM\text{-}INT}$ [kN] (n. Integration)	$R_{d,HERM}$ [kN] Equation (47)	$R_{d,FORM}$ [kN]
Hermite(40.1443, 2.2517, 0.2051, 2.898)	34.0463	34.2636	33.3048
Hermite(40.1513, 2.3351, −0.0781, 3.6634)	31.8476	31.8312	33.0523
Hermite(40.1611, 2.4039, −0.4164, 5.5009)	29.0760	29.0463	32.8532
Hermite(40.1702, 2.4539, −0.6821, 6.7349)	27.5294	27.4957	32.7103

Parameters of Hermite PDF are obtained using calibration of moments in Table 2. $R_{d,HERM\text{-}INT}$ is calculated by numerical integration from the Hermite PDF.

In Table 3, several modelling specifics deserve mention. In Table 2, skewness of 0.2161 and kurtosis of 3.0073 do not satisfy the admissibility condition in Equation (27). Therefore, the lower branch was used. This approach reproduces the target moments with sufficient accuracy, as shown in the first row of Table 3. In this case, a minor calibration was performed using the parameters θ = (40.1443, 2.2517, 0.2051, 2.898) of Hermite PDF, which yields realised moments $M(\theta)$ = (40.1431, 2.2494, 0.2160, 3.0074), practically identical to the moments listed in Table 2. For the other leptokurtic cases ($\alpha_4 > 3$), the first two Hermite parameters match the first two moments in Table 2 exactly, while the third and fourth moments were slightly calibrated. With these settings, all Hermite PDFs in Table 3 reproduce the moments from Table 2 with an accuracy of two decimal places.

In Table 3, the Hermite design resistance differs from the FORM value by about +0.96 kN (2.9%) in the near Gaussian case, whereas it is lower by about 1.22–5.21 kN (3.7–15.9%) in the left-skewed and leptokurtic cases. The Hermite closed-form agrees with numerical integration within about 0.7%.

In Table 3, as skewness becomes more negative and kurtosis increases, the deviation between the design values $R_{d,FORM}$ and $R_{d,HERM}$ increases substantially. This confirms that the FORM approach, which neglects higher-order moments, systematically overestimates the design resistance when the output distribution of R departs from the Gaussian PDF due to negative skewness and higher kurtosis.

The value of $R_{d,HERM}$ is a more accurate estimate of the design resistance compared to $R_{d,FORM}$. For example, the negative skewness and higher kurtosis of the resistance R place more probability mass near smaller values of R. With μ_R and σ_R held constant, these changes reduce the left-hand quantiles of R and thicken the lower tail of the distribution. For independent load effects F, this results in an increased failure probability $P_f = P(F > R)$ relative to the Gaussian model used in FORM with the same μ_R and σ_R. In such cases, the reliability of the design is more accurately ensured by the value of $R_{d,HERM}$, since $R_{d,HERM} < R_{d,FORM}$. If the resulting P_f exceeds the EN 1990 target value of 7.2×10^{-5} for the ultimate limit state, corresponding to the reliability index $\beta_d = 3.8$, the design no longer satisfies the prescribed reliability level.

Under the opposite regime, where $\alpha_{3,R} > 0$ and $\alpha_{4,R} < 3$, the failure probability decreases. With μ_R and σ_R again held constant, the left-hand quantiles of R increase and the lower tail becomes thinner. For independent load effects F, the failure probability $P_f = P(F > R)$ is therefore smaller than for the moment-matched Gaussian model used in FORM, and the 0.12% quantile of R is higher. In this situation, the FORM-based design is conservative.

The results in Table 2 were checked by Monte Carlo simulation using $n = 10^6$ independent samples of $(f_{y1}, r_1, f_{y2}, r_2)$, with inputs as listed in Table 1. For each sample, the resistance R was computed, and the output moments were estimated. The comparison between Tables 2 and 4 shows agreement to three significant digits for both μ_R^* and σ_R^*. The estimates $|\alpha_{3,R}^*|$ and $\alpha_{4,R}^*$ in Table 4 are smaller, which is consistent with finite-sample estimation in cases where the distribution of R exhibits a heavy lower tail. In Monte Carlo

sampling, empirical kurtosis converges slowly because it is driven by rare tail events, and the convergence of extreme quantile estimates is therefore limited by tail sampling.

Table 4. Monte Carlo analysis of output statistics of R and design value $R_{d,FORM}$.

Input Model for Radius r	μ_R^* [kN]	σ_R^* [kN]	$\alpha_{3,R}^*$ [kN]	$\alpha_{4,R}^*$ [kN]	$R_{d,FORM}$ [kN]
Gauss(5, 0.1021)	40.1388	2.2484	0.2158	3.0188	33.3037
Hermite(5, 0.1021, −1, 4)	40.1458	2.3343	−0.0510	3.3672	33.0496
Hermite(5, 0.1022, −2, 5)	40.1583	2.3928	−0.3085	3.9855	32.8843
Hermite(5, 0.1025, −3, 6)	40.1692	2.4346	−0.5002	4.6400	32.7681

$\mu_R^*, \sigma_R^*, \alpha_{3,R}^*, \alpha_{4,R}^*$ denote moments of R evaluated by Monte Carlo method with $n = 1 \times 10^6$ runs.

Figure 15 shows the design value $R_{d,MC}$. It is defined as the empirical 0.12% quantile and corresponds to the 1200th member in the ascending order of the Monte Carlo sample of R for $n = 10^6$.

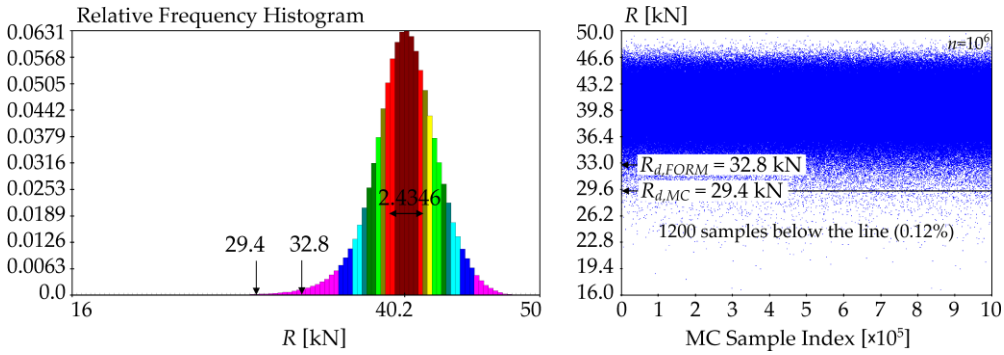

Figure 15. Histogram and Monte Carlo Runs of the Resistance R for the Case $(\alpha_{3,r}, \alpha_{4,r}) = (-3, 6)$.

The estimate $R_{d,MC} = 29.4$ kN is higher than $R_{d,HERM\text{-}INT} \approx R_{d,HERM} \approx 27.5$ kN in Table 3, which is consistent with the lower sample kurtosis $\alpha_{4,R}^* = 4.64$ in Table 4, compared with $\alpha_{4,R}^* = 7.85$ in Table 2. A smaller realised kurtosis implies a less heavy lower tail and, therefore, a higher empirical 0.12% quantile.

6. Discussion

This work provides a Hermite-based framework suitable for reliability analysis and the limit states method. A closed-form expression for the design quantile under a Hermite PDF was derived for both resistance and load effects. The formulation uses the Gaussian design quantile as an input and produces the Hermite design value through a calibrated cubic translation. Agreement with numerical integration is within two per mille in all cases examined, validating the analytical construction. The closed-form expressions are provided in Equations (47) and (48). Admissibility and implementation rules for the Hermite PDF were also established. The monotonicity bound, the positivity check for the lower branch, and the balanced Jacobian for the upper branch form a practical checklist for engineering use.

The case study demonstrates the significant influence of higher-order moments in the limit state method. The input quantities were the yield strength f_y and the radius r of a circular cross-section, while the output quantity was the structural resistance R. The mean resistance changed negligibly across all scenarios, whereas the standard deviation increased by approximately nine percent as the input radius moved toward negative skewness and higher kurtosis. For the most leptokurtic setting, the Hermite design resistance was 27.4957 kN, compared with the FORM value of 32.7103 kN based on the same mean and

standard deviation. This result confirms that neglecting skewness and kurtosis can lead to a non-conservative design when lower tails become heavier.

The Sobol sensitivity analysis showed that the variance of R is strongly influenced by the shape of the distribution of r, even when the first two moments are fixed. As kurtosis increased and skewness became more negative, the first-order sensitivity indices of r increased, while the higher-order remainder decreased. The total Sobol indices quantified the overall contribution of each input r and f_y to the variance of R. In the most skewed and heavy-tailed case of r, the total indices for r and f_y were nearly equal. This finding highlights that the distributional characteristics of r can significantly thicken the lower tail of R and thereby reduce the structural reliability.

Monte Carlo simulation with one million samples confirmed the mean values and standard deviations but yielded smaller magnitudes of skewness and kurtosis, consistent with the slow convergence of tail quantiles and higher-order moments. The 0.12% quantile obtained from Monte Carlo (29.4 kN) was higher than the Hermite design value (27.5 kN), owing to the smaller kurtosis realised in the simulated sample compared with the calibrated analytical model. The FORM design value remained higher than both quantile estimates. These results demonstrate that standard Monte Carlo simulation may be inadequate when higher-order moments significantly influence reliability, as the estimation of tail quantiles and higher-order moments converges slowly. Importance sampling or tail-focused variance-reduction techniques are therefore recommended for future validation of very small quantiles.

It can be concluded that a FORM design value based solely on μ and σ may be insufficient whenever R or F depart from the Gaussian PDF, whether that departure arises from non-Gaussian inputs or from model mappings of Gaussian inputs. In such cases, a calibrated Hermite PDF should be considered, accompanied by admissibility checks and, where necessary, a brief numerical refinement of the input parameters to reproduce the target moments accurately. If R or F depart from the Gaussian PDF through skewness and kurtosis and exhibit a lower or upper tail, the Hermite quantile defined by Equations (47) and (48) should be reported alongside the FORM value.

In engineering applications, the results of the reliability analysis depend on how well the input PDFs reproduce skewness and kurtosis. For the two input random material characteristics studied (yield strength and ductility), the results show that the cubic Hermite polynomial model can represent the shape of the histogram with high accuracy. When the four input moments of the Hermite PDF are interpreted as density parameters, numerical adjustment of these parameters can bring the realised four moments of the Hermite PDF into close agreement with the moments of the approximated histogram. For small skewness and kurtosis, the prescribed parameters of the Hermite PDF are close to the realised moments of the Hermite PDF. Although the derivation treats the first four moments as parameters of the Hermite PDF, the assumption of small skewness and kurtosis need not hold in technical applications. On the lower branch, the realised first four moments of the Hermite PDF may differ slightly from the prescribed targets. For the lower branch (platykurtosis), fitting of the Hermite PDF to an empirical histogram was demonstrated for yield strength. The example showed that numerical tuning of the Hermite parameters can yield an excellent approximation, as confirmed by goodness-of-fit tests. On the upper branch (leptokurtosis), the first two moments are matched exactly, while small deviations may appear in the third and fourth moments. For this branch, fitting of the Hermite PDF to an empirical histogram was demonstrated for steel ductility.

7. Conclusions

A Hermite-based framework for reliability assessment within the limit states method was presented. A closed-form expression for the design quantile under a Hermite density was derived and shown to agree closely with results obtained by numerical integration. Admissibility and implementation conditions were defined, providing a practical checklist for engineering applications.

The closed-form Hermite design quantiles are backward compatible. In the Gaussian limit $\alpha_3 \to 0$ and $\alpha_4 \to 3$, they reduce to the FORM design values [1], allowing the method to be incorporated without disrupting existing design practice. Under extreme input conditions, the Hermite model can produce useful light-tailed or even bimodal shapes; however, such cases require explicit verification of normalisation and positivity before use.

The case study demonstrated that departures from Gaussian behaviour due to skewness and kurtosis can significantly reduce the design resistance when the lower tail becomes pronounced. Variance-based sensitivity analysis showed that the distributional shape of the model inputs can influence the variance of the structural response even when the first two moments are fixed. The convergence of estimators for tail quantiles and higher-order moments was found to be slow under basic Monte Carlo simulation. For very small quantiles, tail-focused importance sampling or subset simulation is recommended.

In engineering practice, the Hermite design quantile should be reported together with the FORM design value based on the mean and the standard deviation, and the associated failure probability should be checked against the target reliability specified in the relevant design code. Hermite-based quantiles are recommended when measured inputs or model outputs exhibit non-negligible skewness or excess kurtosis and when tail quantiles govern the design. In contrast, Gaussian and FORM-based values remain sufficient when such departures are not supported by data. Before use, admissibility should be confirmed using Equation (25) or Equation (27), followed by verification of non-negativity and numerical normalisation, with Figure 8 providing a practical screening map in the (α_3, α_4) plane.

Further developments are expected to focus on dependent input variables, joint non-Gaussian models for resistance and load effects, and direct calibration to target quantiles using efficient variance-reduction techniques.

Funding: The author acknowledges the support from the bilateral Lead Agency project GAČR/NCN No. 25-14337L/No. 2023/51/I/ST11/00069, funded by the Czech Science Foundation and the National Science Centre, Poland, under the OPUS call in the Weave programme. This research was also co-funded by the European Union under the project INODIN, No. CZ.02.01.01/00/23_020/0008487.

Data Availability Statement: The source code used to compute the Sobol sensitivity indices is archived on Zenodo: https://doi.org/10.5281/zenodo.17609078 (accessed on 14 November 2025). The dataset used for the histogram fitting in Figures 4 and 5 is publicly available on Zenodo at https://doi.org/10.5281/zenodo.17936612 (accessed on 15 December 2025). The original contributions presented in this study are included in the article. Further inquiries can be directed to the corresponding author.

Conflicts of Interest: The author declares no conflicts of interest.

Abbreviations

The following abbreviations are used in this manuscript:

Acronym	Definition
cdf	cumulative distribution function
EN 1990	Eurocode 1990: Basis of Structural Design
FORM	First Order Reliability Method
GSA	Global Sensitivity Analysis

MC	Monte Carlo simulation
PDF	probability density function
RC2	Reliability Class 2
SSA	Sobol Sensitivity Analysis

Appendix A

This appendix provides the explicit algebraic steps showing how the transformation in Equation (15) eliminates the quadratic term and reduces the cubic mapping in Equation (7) to the depressed form given in Equation (16).

Starting from Eqution (7):

$$y = \frac{Y}{k_t} = U + \widetilde{h}_3\left(U^2 - 1\right) + \widetilde{h}_4\left(U^3 - 3U\right), \tag{A1}$$

expand and rearrange all terms to one side:

$$\widetilde{h}_4 U^3 + \widetilde{h}_3 U^2 + \left(1 - 3\widetilde{h}_4\right)U - \left(\widetilde{h}_3 + y\right) = 0. \tag{A2}$$

Introduce the shift

$$U = X - A, \tag{A3}$$

and substitute it into (A2). After expanding $(X - A)^3$ and $(X - A)^2$, and collecting terms in powers of X, one obtains:

$$\widetilde{h}_4 X^3 + \left(\widetilde{h}_3 - 3A\widetilde{h}_4\right)X^2 + \left(3A^2\widetilde{h}_4 - 2A\widetilde{h}_3 + 1 - 3\widetilde{h}_4\right)X + \left(-A^3\widetilde{h}_4 + A^2\widetilde{h}_3 + 3A\widetilde{h}_4 - A - \widetilde{h}_3 - y\right) = 0 \tag{A4}$$

Equation (A4) is a general cubic in X. To remove the quadratic term, choose A such that

$$\widetilde{h}_3 - 3A\widetilde{h}_4 = 0 \;\Rightarrow\; A = \frac{\widetilde{h}_3}{3\widetilde{h}_4}, \tag{A5}$$

which corresponds exactly to the Winterstein auxiliary parameter definition in Equation (15). With this choice of A, the term multiplying X^2 vanishes identically, and (A4) reduces to a depressed cubic:

$$X^3 + 3QX - 2\xi = 0, \tag{A6}$$

where the coefficients Q and ξ are those defined in Equation (15).

Appendix B

```
// Inputs: x point, m mean, S st.dev., al3 skewness, al4 kurtosis
// Output: Hermite PDF at x for the selected branch, clamped to zero if negative
// Note: sqrt3(.) is the real cube root used in the Cardano inversion

function HermiteDensity(x, m, S,al3, al4:extended):extended; //Pascal code
var R1, S_, kap, h3, h4, h3_, h4_, y                    :extended;
   A, B, RK, XI, AuxRoot, UX, GaussPdf, Pref            :extended;
Begin                                  // this is a note
h3:=al3/6;
h4:=(al4-3)/24;
if al4 > 3 then
 begin                                        // begin of upper-branch
   h4_:=(sqrt(1 + 36*h4)-1)/18;          a          // h4~, needs 1+36*h4 ≥ 0
   h3_:=h3/(1 + 6*h4_);                    // upper-branch calibration of h3~
```

```
    kap:=1/sqrt(1 + 2*sqr(h3_) + 6*sqr(h4_));          // k_t variance-rescaling factor
    S_:=kap*S;                                          // k_t·S
    y:=(x-m)/S_;
    B:=1/(3.*h4_);                                      // cubic normalisation (Cardano form)
    A:=h3_*B;                                           // linear shift in the depressed cubic
    RK:=sqr(B-1-A*A)*(B-1-A*A);                         // Q^3 (discriminant term)
    XI:=1.5*B*(A + Y)-A*A*A;                            // ξ (Cardano numerator)
    AuxRoot:=Sqrt(XI*XI + RK);                          // R = √(ξ^2 + Q^3), needs ξ^2 + Q^3 ≥ 0
    UX:=sqrt3(AuxRoot + XI)-sqrt3(AuxRoot-XI)-A; // U(y): real Cardano root
    GaussPdf:=exp(-sqr(UX)/2)/sqrt(2*pi);// φ(U)
    Pref:=B/(2*S_);                                     // Jacobian prefactor (B/2)/( k_t·S)
    R1:=GaussPdf*Pref*(((1/sqrt3(sqr(AuxRoot+XI)))*(XI/ AuxRoot+1))+
       ((1/sqrt3(sqr(AuxRoot-XI)))*(1-XI/AuxRoot))); // stable Jacobian (balanced form)
 end                                                    // end of upper-branch
else
 begin                                                  // begin of lower-branch
    h4_:=h4-27*(sqr(h4));                               // lower-branch correction of h̃_4(Winterstein)
    h3_:=h3/(1+24*h4_);                                 // calibrated h̃_3 for first-order regime
    kap:=1/sqrt(1+10*sqr(h3_)+42*sqr(h4_));             // k_t for lower branch
    S_:=kap*S;                                          // k_t·S
    y:=(x-m)/S_;
    UX:=Y-h3_*(Y*Y-1)-h4_*(Y*Y*Y-3*Y); // first-order Neumann inversion U≈...
    GaussPdf:=exp(-sqr(UX)/2)/sqrt(2*pi); // φ(U)
    R1:=(GaussPdf/S_)* (1-2*h3_*Y-3*h4_*(Y*Y-1)); // φ(U)·|dU/dy| (first order)
 end;                                                   // end of lower-branch
if R1 ≥ 0 then Result:=R1 else Result:=0; // defensive clamp in extreme inputs
end; // See Figure 8 for admissible (green), near (yellow), non (red) (α_3, α_4).

// Example call (standardised): fx : = HermiteDensity(0.0, 0.0, 1.0, −1.0, 4.0);
```

References

1. *EN 1990:2002*; Eurocode—Basis of Structural Design. European Committee for Standardization: Brussels, Belgium, 2002.
2. Kamiński, M.; Błoński, R. Analytical and Numerical Reliability Analysis of Certain Pratt Steel Truss. *Appl. Sci.* **2022**, *12*, 2901. [CrossRef]
3. Qin, X.; Kaewunruen, S. Machine learning and traditional approaches in shear reliability of steel fiber reinforced concrete beams. *Reliab. Eng. Syst. Saf.* **2024**, *251*, 110339. [CrossRef]
4. Wang, J.; Ye, X.; Zheng, W.; Liu, P. Improved Calculation of Load and Resistance Factors Based on Third-Moment Method. *Appl. Sci.* **2021**, *11*, 9107. [CrossRef]
5. Liu, H.; Mao, Y.; Zhang, Z.; Yuan, F.; Wang, F. A Second-Order Second-Moment Approximate Probabilistic Design Method for Structural Components Considering the Curvature of Limit State Surfaces. *Buildings* **2025**, *15*, 3421. [CrossRef]
6. Zhao, S.; Zhang, X.; Zhang, C.; Yan, Z.; Zhang, X.; Zhang, B.; Dai, X. Extreme-Value Combination Rules for Tower–Line Systems Under Non-Gaussian Wind-Induced Vibration Response. *Buildings* **2025**, *15*, 1871. [CrossRef]
7. Chen, M.; Yuan, G.; Li, C.B.; Zhang, X.; Li, L. Dynamic Analysis and Extreme Response Evaluation of Lifting Operation of the Offshore Wind Turbine Jacket Foundation Using a Floating Crane Vessel. *J. Mar. Sci. Eng.* **2022**, *10*, 2023. [CrossRef]
8. Cheng, K.; Weng, G.; Cheng, Z. Influence of Load Partial Factors Adjustment on Reliability Design of RC Frame Structures in China. *Sci. Rep.* **2023**, *13*, 7260. [CrossRef]
9. Zhang, M.; Chen, M.; Fang, W.; Li, Q.; Xu, K.; Huang, H.; Feng, Y. Time-Dependent Reliability Estimation of Bridge Structures with Auto-Correlated Stochastic Processes Based on the Gaussian Copula Function. *Mech. Based Des. Struct. Mach* **2025**. [CrossRef]
10. Poutanen, T. Combination of Variable Loads in Structural Design. *Appl. Sci.* **2024**, *14*, 6466. [CrossRef]
11. Kala, Z. Reliability Analysis of the Lateral Torsional Buckling Resistance and the Ultimate Limit State of Steel Beams with Random Imperfections. *J. Civ. Eng. Manag.* **2015**, *21*, 902–911. [CrossRef]

12. Alotaibi, R.; Nassar, M. A New Exponential Distribution to Model Concrete Compressive Strength Data. *Crystals* **2022**, *12*, 431. [CrossRef]
13. Ndeba, B.S.; El Alani, O.; Ghennioui, A.; Benzaazoua, M. Comparative Analysis of Seasonal Wind Power Using Weibull, Rayleigh and Champernowne Distributions. *Sci. Rep.* **2025**, *15*, 2533. [CrossRef]
14. Obulezi, O.J.; Semary, H.E.; Nadir, S.; Igbokwe, C.P.; Orji, G.O.; Al-Moisheer, A.S.; Elgarhy, M. Type-I Heavy-Tailed Burr XII Distribution with Applications to Quality Control, Skewed Reliability Engineering Systems and Lifetime Data. *Comput. Model. Eng. Sci.* **2025**, *144*, 2991–3027. [CrossRef]
15. Qi, Y.; Jiang, B.; Lei, W.; Zhang, Y.; Yu, W. Reliability Analysis of Normal, Lognormal, and Weibull Distributions on Mechanical Behavior of Wood Scrimber. *Forests* **2024**, *15*, 1674. [CrossRef]
16. Boiko, Y.M.; Marikhin, V.A.; Myasnikova, L.P. Tensile Strength Statistics of High-Performance Mono- and Multifilament Polymeric Materials: On the Validity of Normality. *Polymers* **2023**, *15*, 2529. [CrossRef]
17. Elhajjar, R. Fat-Tailed Failure Strength Distributions and Manufacturing Defects in Advanced Composites. *Sci. Rep.* **2025**, *15*, 25977. [CrossRef]
18. Park, K.-H.; Lee, S.-W.; Kim, H.-J.; Lim, J.-S. Reliability Assessment of Statistical Distributions for Analyzing Dielectric Breakdown Strength of Polypropylene. *Appl. Sci.* **2024**, *14*, 3. [CrossRef]
19. Vanem, E.; Gramstad, O.; Babanin, A.; De Bin, R.; Trulsen, K. On the Distribution of Ocean Wave Crest Heights in Varying Wave Conditions. *J. Ocean Eng. Mar. Energy* **2024**, *10*, 797–815. [CrossRef]
20. Luo, H.; Xiong, Q.; Zhang, X.; Zuo, S. Study on the Probabilistic Characteristics of Forces in the Support Structure of Heliostat Array Based on the DBO-BP Algorithm. *Sci. Rep.* **2025**, *15*, 23831. [CrossRef]
21. Zhou, G.; Zhu, Q.; Mao, Y.; Chen, G.; Xue, L.; Lu, H.; Shi, M.; Zhang, Z.; Song, X.; Zhang, H.; et al. Multi-Locus Genome-Wide Association Study and Genomic Selection of Kernel Moisture Content at the Harvest Stage in Maize. *Front. Plant Sci.* **2021**, *12*, 697688. [CrossRef]
22. Sánchez-Pérez, A.; Rodríguez-Sánchez, M.; Martínez-Cáceres, C.M.; Jornet-García, A.; Moya-Villaescusa, M.J. The Efficacy of a Deproteinized Bovine Bone Mineral Graft for Alveolar Ridge Preservation: A Histologic Study in Humans. *Biomedicines* **2025**, *13*, 1358. [CrossRef]
23. Mai, S.H.; Dang, H.-K.; Nguyen, V.T.; Thai, D.-K. Stochastic Nonlinear Inelastic Analysis for Steel Frame Structure Using Monte Carlo Sampling. *Ain Shams Eng. J.* **2023**, *14*, 102527. [CrossRef]
24. Jindra, D.; Kala, Z.; Kala, J. Flexural Buckling of Stainless Steel CHS Columns: Reliability Analysis Utilizing FEM Simulations. *J. Constr. Steel Res.* **2022**, *188*, 107002. [CrossRef]
25. Winterstein, S.R. Nonlinear Vibration Models for Extremes and Fatigue. *J. Eng. Mech.* **1988**, *114*, 1772–1790. [CrossRef]
26. Achamyeleh, T.; Çamur, H.; Savaş, M.A.; Evcil, A. Mechanical strength variability of deformed reinforcing steel bars for concrete structures in Ethiopia. *Sci. Rep.* **2022**, *12*, 2600. [CrossRef]
27. Hu, D.; Zhang, T.; Jin, Q. Investigation of Wind Pressure Dynamics on Low-Rise Buildings in Sand-Laden Wind Environments. *Buildings* **2025**, *15*, 2779. [CrossRef]
28. Li, T.; Yang, Q.; Zhang, C.; Ren, C.; Liu, M.; Zhou, T. A Novel Non-Gaussian Analytical Wake Model of Yawed Wind Turbine. *J. Wind Eng. Ind. Aerodyn.* **2025**, *259*, 106040. [CrossRef]
29. Dundu, M. Mathematical Model to Determine the Weld Resistance Factor of Asymmetrical Strength Results. *Structures* **2017**, *12*, 298–305. [CrossRef]
30. Zhao, Y.-G.; Lu, Z.-H. Estimation of Load and Resistance Factors Using the Third-Moment Method Based on the 3P-Lognormal Distribution. *Front. Archit. Civ. Eng. China* **2011**, *5*, 315–322. [CrossRef]
31. Wang, T.; Ji, X.; Zhao, Y.-G. Structural Reliability Assessment Using Quartic Normal Transformation. *Sci. Rep.* **2025**, *15*, 990. [CrossRef]
32. Mochocki, W.; Obara, P.; Radoń, U. Impact of the Wind Load Probability Distribution and Connection Types on the Reliability Index of Truss Towers. *J. Theor. Appl. Mech.* **2020**, *58*, 403–414. [CrossRef] [PubMed]
33. Zhang, X.-Y.; Zhao, Y.-G.; Lu, Z.-H. Unified Hermite Polynomial Model and Its Application in Estimating Non-Gaussian Processes. *J. Eng. Mech.* **2019**, *145*, 04019001. [CrossRef]
34. Tong, M.-N.; Shen, F.-Q.; Cui, C.-X. The Inverse Transformation of L-Hermite Model and Its Application in Structural Reliability Analysis. *Mathematics* **2022**, *10*, 4318. [CrossRef]
35. Yang, L.; Gurley, K.R.; Prevatt, D.O. Probabilistic Modeling of Wind Pressure on Low-Rise Buildings. *J. Wind Eng. Ind. Aerodyn.* **2013**, *114*, 18–26. [CrossRef]
36. Cheon, D.J.; Kim, Y.C.; Yoon, S.W. Non-Gaussian Properties and Extreme Values of Net Pressure on a Dome with a Central Opening. *J. Build. Eng.* **2025**, *113*, 114022. [CrossRef]
37. Li, J.; Nie, S.; Liu, M.; Yang, Q.; Guo, K. Two Parallel Cable Trusses-Supported Photovoltaic System: Extreme Wind-Induced Response and Displacement-Based Gust Response Factors. *J. Wind Eng. Ind. Aerod.* **2025**, *265*, 106157. [CrossRef]

38. Zhao, Y.-G.; Lu, Z.-H. Fourth-Moment Standardization for Structural Reliability Assessment. *J. Struct. Eng.* **2007**, *133*, 916–924. [CrossRef]
39. Li, Z.-P.; Hu, D.-Z.; Zhang, L.-W.; Zhang, Z.; Shi, Y. L-Moments-Based FORM Method for Structural Reliability Analysis Considering Correlated Input Random Variables. *Buildings* **2023**, *13*, 1261. [CrossRef]
40. Low, Y.M. A New Distribution for Fitting Four Moments and Its Applications to Reliability Analysis. *Struct. Saf.* **2013**, *42*, 12–25. [CrossRef]
41. Xu, J.; Ding, C. Adaptive Hermite Distribution Model with Probability-Weighted Moments for Seismic Reliability Analysis of Nonlinear Structures. *ASCE–ASME J. Risk Uncertain. Eng. Syst. Part A Civ. Eng.* **2021**, *7*, 04021052. [CrossRef]
42. Denoël, V. Moment-Based Hermite Model for Asymptotically Small Non-Gaussianity. *Appl. Math. Model.* **2025**, *144*, 116061. [CrossRef]
43. Zhao, Z.; Lu, Z.-H.; Zhao, Y.-G. Simulating Non-Stationary and Non-Gaussian Cross-Correlated Fields Using Multivariate Karhunen–Loève Expansion and L-Moments-Based Hermite Polynomial Model. *Mech. Syst. Signal Process.* **2024**, *216*, 111480. [CrossRef]
44. Lu, Y.; Pang, R.; Zhou, Y.; Jiang, S.; Xu, B. A Novel Method for Simulating Large-scale 3D Non-Gaussian Random Fields in Geotechnical Engineering. *Comput. Geotech.* **2026**, *189*, 107621. [CrossRef]
45. Kim, J.H.T.; Kim, H. Estimating Skewness and Kurtosis for Asymmetric Heavy-Tailed Data: A Regression Approach. *Mathematics* **2025**, *13*, 2694. [CrossRef]
46. Zhao, Y.-G.; Zhang, X.-Y.; Lu, Z.-H. A Flexible Distribution and Its Application in Reliability Engineering. *Reliab. Eng. Syst. Saf.* **2018**, *176*, 1–12. [CrossRef]
47. Zhao, Z.; Lu, Z.-H.; Li, C.-Q.; Zhao, Y.-G. Dynamic Reliability Analysis for Non-Stationary Non-Gaussian Response Based on the Bivariate Vector Translation Process. *Probab. Eng. Mech.* **2021**, *66*, 103143. [CrossRef]
48. Cui, S.; Hong, L. Study of the Kurtoses Transmission of Linear Structures under Stationary Non-Gaussian Random Loadings. *J. Vib. Control* **2025**, *31*, 1438–1456. [CrossRef]
49. Cui, S.; Hong, L.; Zang, L. Research on Response Kurtosis Estimation in Linear Structures Subjected to Nonstationary Random Excitation: An Envelope-Based Method. *Shock Vib.* **2024**, *2024*, 9998563. [CrossRef]
50. Ma, X.; Liu, Z. Influence of Ground Motion Non-Gaussianity on Seismic Performance of Buildings. *Buildings* **2024**, *14*, 2364. [CrossRef]
51. Sheng, X.; Yu, K.; Fan, W.; Xin, S. Frequency-Domain Analysis and Dynamic Reliability Assessment of Random Vibration for Non-Classically Damped Linear Structure under Non-Gaussian Random Excitations. *Reliab. Eng. Syst. Saf.* **2025**, *264*, 111363. [CrossRef]
52. Zhu, Y.; Yao, W. A Conditional Probability Density Function Model for Fatigue Damage Estimation in Broadband Non-Gaussian Stochastic Processes. *Int. J. Fatigue* **2025**, *197*, 108958. [CrossRef]
53. Cui, S.; Chen, S.; Li, J.; Wang, C. Estimation of Fatigue Damage under Uniform-Modulated Non-Stationary Random Loadings Using Evolutionary Power Spectral Density Decomposition. *Mech. Syst. Signal Process.* **2025**, *226*, 112334. [CrossRef]
54. Trapp, A.; Wolfsteiner, P. Fast Assessment of Non-Gaussian Inputs in Structural Dynamics Exploiting Modal Solutions. *Mech. Syst. Signal Process.* **2025**, *228*, 112396. [CrossRef]
55. Sodahl, N.; Skrede, S.O.; Grytoyr, G.; Gregersen, K. Fatigue Damage Summation with Bias Correction. *Mar. Struct.* **2026**, *105*, 103926. [CrossRef]
56. Dai, S.; Sweetman, B.; Tang, S. Impact of Non-Gaussian Winds on Blade Loading and Fatigue of Floating Offshore Wind Turbines. *J. Mar. Sci. Eng.* **2025**, *13*, 1686. [CrossRef]
57. Li, Y.; Xu, J. Novel Hermite Polynomial Model Based on Probability-Weighted Moments for Simulating Non-Gaussian Stochastic Processes. *J. Eng. Mech.* **2024**, *150*, 04024006. [CrossRef]
58. Zhao, Y.-G.; Wang, T.; Ji, X.; Huang, G. Quartic Hermite polynomial model-based translation method for extreme wind load estimation. *J. Wind Eng. Ind. Aerodyn.* **2024**, *245*, 105653. [CrossRef]
59. Ianculescu, D.; Anghel, C.G. Innovative Explicit Relations for Weibull Distribution Parameters Based on K-Moments. *Mathematics* **2025**, *13*, 3473. [CrossRef]
60. Braun, M.; Neuhäusler, J.; Denk, M.; Renken, F.; Kellner, L.; Schubnell, J.; Jung, M.; Rother, K.; Ehlers, S. Statistical Characterization of Stress Concentrations along Butt Joint Weld Seams Using Deep Neural Networks. *Appl. Sci.* **2022**, *12*, 6089. [CrossRef]
61. Bazaras, Ž.; Lukoševičius, V.; Bazaraitė, E. Structural Materials Durability Statistical Assessment Taking into Account Threshold Sensitivity. *Metals* **2022**, *12*, 175. [CrossRef]
62. Qin, H.; Ka, T.A.; Li, X.; Sun, K.; Qin, K.; Noor E Khuda, S.; Tafsirojjaman, T. Evaluation of Tensile Strength Variability in Fiber Reinforced Composite Rods Using Statistical Distributions. *Front. Built Environ.* **2025**, *10*, 1506743. [CrossRef]
63. Adamu, M.; Rehman, K.U.; Ibrahim, Y.E.; Shatanawi, W. Predicting the Strengths of Date Fiber Reinforced Concrete Subjected to Elevated Temperature Using Artificial Neural Network and Weibull Distribution. *Sci. Rep.* **2023**, *13*, 18649. [CrossRef] [PubMed]

64. Bezerra de Lima, N.; Pontes, M.; Silva, D.; Manta, R.C.; Teti, B.S.; Nascimento, H.C.B.; Santos, L.B.T.; Lima, N.B. Evaluation of Probability Distributions in the Study of Characteristic Compressive Strength of Metakaolin Concrete Blocks. *Ambiente Construído* **2025**, *25*, e138069. [CrossRef]
65. Vu, C.-C.; Ho, N.-K. Best Fit of Statistical Distribution to Compressive Strength of Green Concrete Produced in the Northern area of Vietnam. *J. Eng. Res.* **2025**, *13*, 1403–1413. [CrossRef]
66. Melcher, J.; Kala, Z.; Holický, M.; Fajkus, M.; Rozlívka, L. Design Characteristics of Structural Steels Based on Statistical Analysis of Metallurgical Products. *J. Constr. Steel Res.* **2004**, *60*, 795–808. [CrossRef]
67. Kala, Z.; Melcher, J.; Puklický, L. Material and Geometrical Characteristics of Structural Steels Based on Statistical Analysis of Metallurgical Products. *J. Civ. Eng. Manag.* **2009**, *15*, 299–307. [CrossRef]
68. Brockenbrough, R.L. *MTR Survey of Plate Material Used in Structural Fabrication—Final Report, Part A: Yield–Tensile Properties*; American Institute of Steel Construction (AISC): Chicago, IL, USA, 2001.
69. Kala, Z. Sensitivity Analysis in Probabilistic Structural Design: A Comparison of Selected Techniques. *Sustainability* **2020**, *12*, 4788. [CrossRef]
70. Fakharian, P.; Naderpour, H.; Sharbatdar, M.K.; Ghasemi, S.H. Advancements in structural target reliability: A comprehensive examination of theories and practical applications (2013–2024). *Structures* **2024**, *66*, 106930. [CrossRef]
71. Panther, L.; Wagner, W.; Freitag, S. A Consistently Linearized Spectral Stochastic Finite Element Formulation for Geometric Nonlinear Composite Shells. *Comput. Mech.* **2025**, *75*, 1655–1683. [CrossRef]
72. Puman, E.; Lellep, J. Analysis of Elastic Conical Shells of Variable Thickness with Rib-reinforcement. *Acta Comment. Univ. Tartu. Math.* **2025**, *29*, 5–14. [CrossRef]
73. Benasciutti, D.; Tovo, R. Frequency-based Analysis of Random Fatigue Loads: Models, Hypotheses, Reality. *Mater. Wiss. Werksttech.* **2018**, *49*, 345–367. [CrossRef]
74. *EN 10060:2003+A1:2008*; Hot Rolled Round Steel Bars for General Purposes—Dimensions and Tolerances on Shape and Mass. European Committee for Standardization (CEN): Brussels, Belgium, 2008.
75. Kala, Z.; Valeš, J.; Jönsson, J. Random Fields of Initial Out of Straightness Leading to Column Buckling. *J. Civ. Eng. Manag.* **2017**, *23*, 902–913. [CrossRef]